

ENabling Optimized DISruptivE airframe-propulsion integration concepts

H2020 Research and Innovation Action
Grant Agreement No 860103

Deliverable Reference Number: D3.7

Deliverable Title:
WP3 Final Public Report

Lead participant: UTWE
Contributing participant(s): UBRI,TUD,ECL,VKI

30 September 2023

Start date of project: 1st of June 2020
Duration: 48 months

Type		
R	Document, report	X
DEM	Demonstrator, pilot, prototype, etc.	
DEC	Websites, patent fillings, videos, etc.	
ORDP	Open Research Data Pilot	
Dissemination Level		
PU	Public	X
CO	Confidential, only for members of the consortium (incl. Commission Services)	

APPROVAL

Title	Issue	Revision
WP3 Final Public Report	1	0

Author(s)	Date
Leandro Castelucci (UTWE) Ismaeel Zaman(UBRI) Fernanda Monteiro(TUD) Daniel Acevedo Giraldo(ECL) Hasse Dekker (TUD/NLR) Erica Gallo (VKI)	29/09/2023

Approved by	Date
Leandro Castelucci	30/09/2023

Contents

1 Introduction **5**

2 Configuration A1: UTWE **6**
2.1 Experimental Setup . . . 6
2.2 Experimental campaigns . . . 6
2.2.1 Inflow characterization . . . 6
2.2.2 Performance . . . 7
2.2.3 Far-field acoustics . . . 7
2.2.4 Near-field acoustics . . . 7
2.3 Main results . . . 8
2.4 Main Achievements . . . 9
2.5 Deliverables . . . 9
2.6 Dissemination . . . 9

3 Configuration A1: UBRI **11**
3.1 Experimental Setup . . . 11
3.2 Experimental campaign . . . 11
3.3 Main results . . . 12
3.4 Main Achievements . . . 13
3.5 Deliverables . . . 14
3.6 Dissemination . . . 14

4 Configuration A2 **14**
4.1 Experimental Setup . . . 14
4.2 Experimental campaigns . . . 15
4.3 Main results . . . 16
4.4 Main Achievements . . . 18
4.5 Deliverables . . . 18
4.6 Dissemination . . . 18

5 Configuration B1 **19**
5.1 Experimental Setup . . . 19
5.2 Experimental campaigns . . . 19
5.3 Main results . . . 21
5.4 Main Achievements . . . 22
5.5 Deliverables . . . 22
5.6 Dissemination . . . 22

6 Configuration B2 **24**
6.1 Experimental Setup . . . 24
6.2 Experimental campaigns . . . 25
6.3 Main results . . . 26
6.3.1 Aerodynamic Performances . . . 26
6.3.2 Far-Field Sound Inspection . . . 27
6.4 Main Achievements . . . 29
6.5 Deliverables . . . 30

6.6 Dissemination 30

7 Configuration B3-VTOL **31**
7.1 Experimental Setup 31
7.2 Experimental campaigns 31
7.3 Main results 31
7.4 Main Achievements 32
7.5 Deliverables 33
7.6 Dissemination 34

8 Configuration B3-Flap **35**
8.1 Experimental Setup 35
8.2 Experimental campaigns 35
8.3 Main results 35
8.4 Main Achievements 37
8.5 Deliverables 37
8.6 Dissemination 38

9 Configuration C **39**
9.1 Experimental Setup 39
9.2 Experimental campaigns 39
9.3 Main results 40
9.4 Main Achievements 43
9.5 Deliverables 43
9.6 Dissemination 44

10 Conclusion **44**

1 Introduction

Task 3.1 (UTWE,UBRI) covers the experimental campaigns of the Boundary Layer Ingestion (BLI) Configurations A1 and A2. Configuration A1 refers to the ingestion of a zero-pressure gradient boundary layer (ZPG) into an open propeller, while A2 refers to the ingestion of an adverse-pressure gradient boundary layer (APG) representing the partially buried propulsion installation arrangement. UTWE conducted the A1 configuration while UBRI conducted both A1 and A2 configurations. The extensive datasets gathered independently from both partners across a wide range of far-field acoustic, flow survey, surface pressure, and propeller force instrumentation will permit insights into the acoustic characteristics of BLI over several parameters, and form a cohesive dataset to inform the numerical partners of WP4 for simulation initialization and validation.

The focus of **Task 3.2 (TUD,ECL)** is here placed on the viscous and potential interactions that take place in DEP systems when the propulsors are distributed upstream or downstream of the wing and on finite-chord scattering effects including shielding. Both propeller-propeller and propeller-wing interactions will be considered by varying the relative positions of those components. As in Task 3.1, the acoustic emissions will be weighed against power efficiency, and the insight that will be gained on the flow and noise physics will support the validation of the CFD/CAA simulations performed in WP4 and the interpretation of the results of the optimization in WP5. TUD conducted the experiments with the B1 configuration whereas ECL evaluated the B2 and NLR the B3.

In the framework of **Task 3.3 (VKI)**, an aeroacoustic test rig conceived for the study of single and coaxial propeller propulsive system for drone applications had been developed. The experimental setup, designed and commissioned at the ALCOVES anechoic laboratory of von Karman Institute for Fluid Dynamics, Belgium, is equipped with aerodynamic sensors, enabling performance analysis. A squared microphone antenna is used for noise characterization. The versatility lies in the opportunity to explore different parameters such as distance between rotors in a specific range, and rotational speed. Requirements for the qualification of the test room consist of low-level background noise, as well as low-level turbulence intensity and uniformity. Hence, validation checks to differentiate background noise sources are reported. The generated database comprises the aerodynamic and acoustic characterization of Mejzlik 2-blade propellers. Eventually, the benchmark is meant to support the validation of low- and high-fidelity numerical methods.

2 Configuration A1: UTWE

2.1 Experimental Setup

The following experiments were conducted in the University of Twente Wind Tunnel. The test section has a $0.9 \times 0.7\ m^2$ rectangular area, and it is inside a 160 Hz cutoff anechoic chamber. Detailed information about the facility can be found in [1]. The experimental setup consists of a propulsive setup to drive a propeller (detailed information about the system can be found in D3.3) mounted on top of a flat plate, as shown in Figure 1

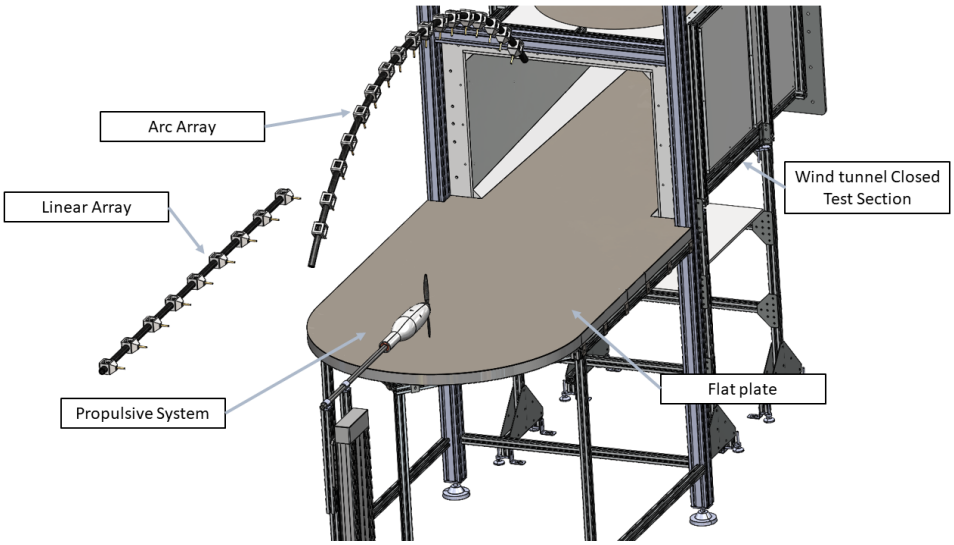

Figure 1: Schematics of the experimental at UTWE

The propulsive system drive a Meijzlik 12" × 18", two-bladed propeller, immersed in a non-uniform inflow. The propeller has a diameter D = 304.8 m. The inflow is changed by using 2 different tripping devices, resulting in three configurations. The effects of clearance (distance between propeller tip and flat plate), RPM, and different inflows is analysed.

2.2 Experimental campaigns

The parameters varied during the experiments are summarized in Table 1

Table 1: Parameters varied during the experiments.

WT Speed	RPM	Clearance	Tripping	Inflow
30 m/s	4000 to 8000	5,10,20 mm	No trip Trip 1 Trip 2	Isolated Immersed

2.2.1 Inflow characterization

The boundary layer impinging on the propeller is controlled by 60° zigzag tripping devices positioned 3620 mm upstream of the propeller plane. The tripping device height controls the boundary layer thickness. Trip 0 is the flat plate. Trip 1 and Trip 2 have 8 mm and 12 mm trip heights, respectively. The boundary layer thickness in each experiment determines the immersion level of the propeller blades. An immersion ratio ranging from 18% to 45% is possible. Table 2 shows the main characteristics of each boundary layer at the propeller plane.

Table 2: Boundary layer characteristics for each tripping device. δ is the boundary layer thickness, δ/D is the immersion ratio, $H = \delta^*/\theta$ is the shape factor (δ^* is the displacement thickness and θ is the momentum thickness), Re_x is the Reynolds of the stream-wise position from the tripping X, and Re_θ is the Reynolds number for the momentum thickness

Trip	δ, mm	δ/D	H	Re_x	Re_θ
Trip 0	54.5	0.18	1.32	7.28×10^6	18550
Trip 1	102.5	0.34	1.27	7.29×10^6	22370
Trip 2	139.8	0.46	1.24	6.82×10^6	33920

2.2.2 Performance

Throughout all the experimental campaigns, the system is connected to a *FUTEK MBA500* bi-axial load cell (222 N; 5.65 Nm) which account for Thrust and Torque of the propeller on the shaft of the motor. A spectral analysis of the performance response of the propeller was also acquired, to understand possible changes in loads due to the immersion.

2.2.3 Far-field acoustics

Two arrays of microphones are positioned with the center microphone pointed at the propeller plane. The array facing the plate is an arc array with 17 microphones, ranging from 40 degrees (upstream) to 140 degrees (downstream). The side array is a linear array with 10 microphones from 60 degrees to 110 degrees. Both arcs are spaced 1.50m (4.9D) from the center of the propeller. The arrays use G.R.A.S.40 PH free-field microphones connected to the arc through 3d-printed inserts.

2.2.4 Near-field acoustics

An instrumented flat plate is positioned underneath the propeller - by modifying the original flat plate - and the near-field noise is captured by 0.5 mm diameter pinholes attached to a remote microphone probe (RMP) setup through a 1.6 mm channel. Each pinhole leads to a *Knowles FG-23329-P07* microphone. Steady pressures are measured by connecting the anechoic end of the RMP setup to the pressure scanner *NetScanner 9216*. Both near-field and far-field microphone data are acquired by a *PXIe-4499* Sound and Vibration module (NI PXIe-1073 chassis).

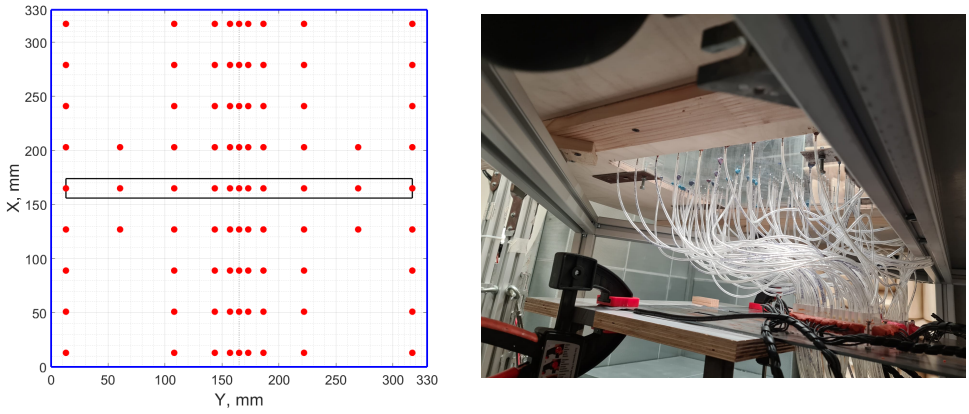

Figure 2: (Right) Schematics of the instrumented plate. The red dots are the positions of the pinholes. Black rectangle is the propeller wetted area.(Left) Bottom view of the setup showing the flexible tubes connection with the Knowles microphones.

2.3 Main results

The main results of the Configuration A1 (UTWE) are the influence of the immersion of the propeller in a non-uniform inflow on noise, the comparison between the two arrays of microphones and the effects of the propeller on the incoming flow.

The comparison of the results for different conditions showed that the immersion in the boundary layer had a significant influence on the noise generated by the propeller, with increases of up to 6 dB in the overall noise (Figure 3). Further, the directivity pattern was also affected by the immersion. The results showed that the downstream directivity was more affected by the noise increase, in comparison with the isolated propeller (Figure 4).

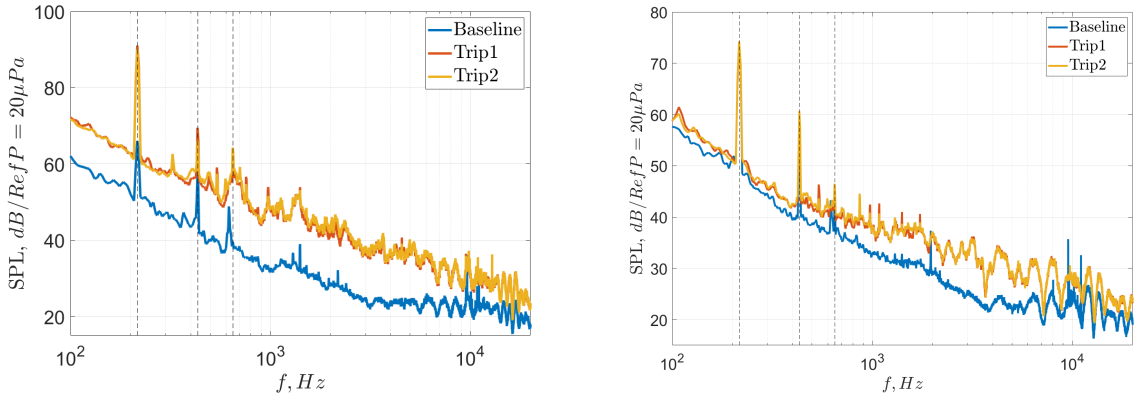

Figure 3: Noise levels comparison between baseline and tripped configurations.(Right) Arc array on top. (Left) Linear array on the side. Measurement of central microphone ($\theta = 90$)

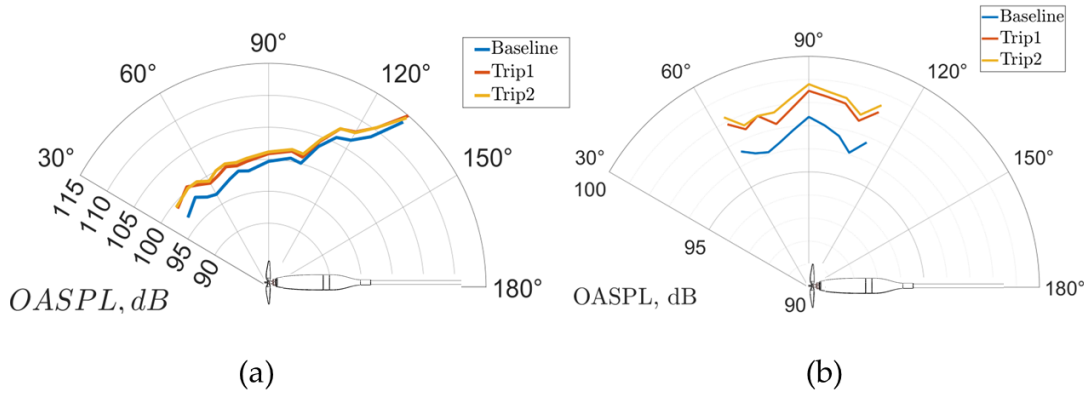

Figure 4: Directivity results for both tripping devices ($U = 33m/s, RPM = 6500$). Arc-array results are shown in (a) and linear-array are shown in (b).

The unsteady pressure analysis shows the regions of influence of the propeller on the turbulent struc-

tures of the flow (Figure 5). Downstream there is an increase in the correlation length of the turbulent structures inflicted by the propeller. This increase is dependent on the direction of rotation of the propeller (right and left sides of rotation). The changes in the correlation length for the blade rotating towards the plate are not related with boundary layer thickness, therefore it is not the leading parameter in the effect.

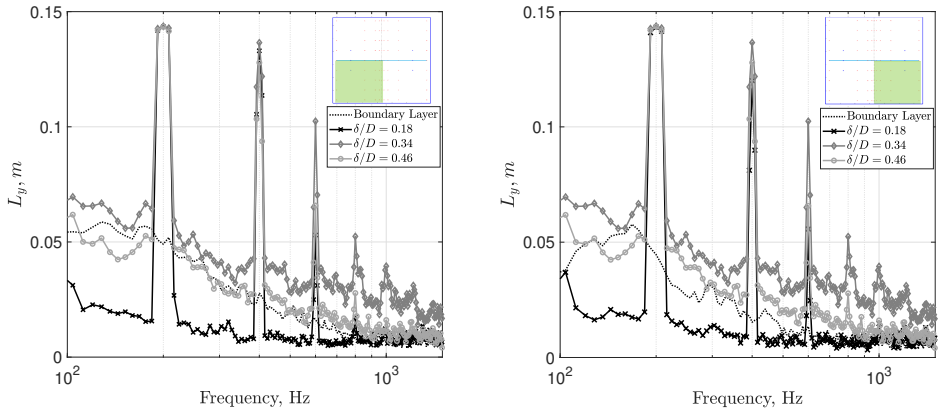

Figure 5: Correlation length with comparison between BLI immersions (6000 rpm, J = 0.98). Dashed line is the $\delta/D = 0.46$ boundary layer. Green squares showing regions on the plate.

2.4 Main Achievements

One of the main accomplishments was the design and construction of a rig capable of driving a propeller, measuring both loads and the precise position of the blades. All the measurement techniques and equipment will be valuable for the current work and future research involving rotors and propellers.

The extensive dataset created with the many experiments was documented and shared with other Work Packages for result comparison, simulations, and models. The experiments successfully accessed the performance, noise characteristics, and effects on the flow and surface of the propeller mounted on the flat plate. Further, data comparison between different wind tunnels (UTWE, UBRI) will be valuable to understanding the effects and the main parameters involved in the noise mechanism of Configuration A1.

2.5 Deliverables

Completed deliverables:

- D3.3: Configuration A experimental databases (without mitigation)
- D3.6: Documentation of experimental databases (without mitigation)
- D3.7: WP3 final public report (current document)

2.6 Dissemination

All experimental datasets are uploaded on Zenodo repository, DOI DOI `https://doi.org/10.5281/zenodo.7940856`.

Additionally, the following conference publications were also finished and presented:

- Castelucci, Leandro A., Cornelis H. Venner, and Leandro D. de Santana. "Experimental analysis of the noise of small propellers subjected to non-uniform inflow." AIAA SCITECH 2023 Forum. 2023.

- Castelucci, Leandro A., and Cornelis H. Venner. "Propeller influence on surface pressure fluctuation under boundary layer ingestion condition". 52nd International Congress and Exposition on Noise Control Engineering, INTERNOISE 2023.
- Castelucci, Leandro A., Cornelis H. Venner, and Ysbrand H. Wijnant. "Experimental study of surface noise mitigation for propellers in boundary layer ingestion configuration." FORUM ACUSTICUM 2023.

3 Configuration A1: UBRI

3.1 Experimental Setup

The objectives of this task constituted the generation of a comprehensive experimental dataset regarding the A1 configuration at the Aeroacoustic Facility at UBRI using a purpose-built experimental setup. The data would contain far-field acoustic data, near-field surface pressure, propeller forces, flow velocity surveys and synchronised blade position information across a wide range of operational parameters.

This data would then be used to draw inferences into the acoustic properties of BLI of a ZPG boundary layer and serve as inputs to the numerical partners. Portions of the dataset are to be published. Full details of the experimental setup and instrumentation used at UBRI for this campaign can be found in D3.6 and D3.3. A brief overview will be given here.

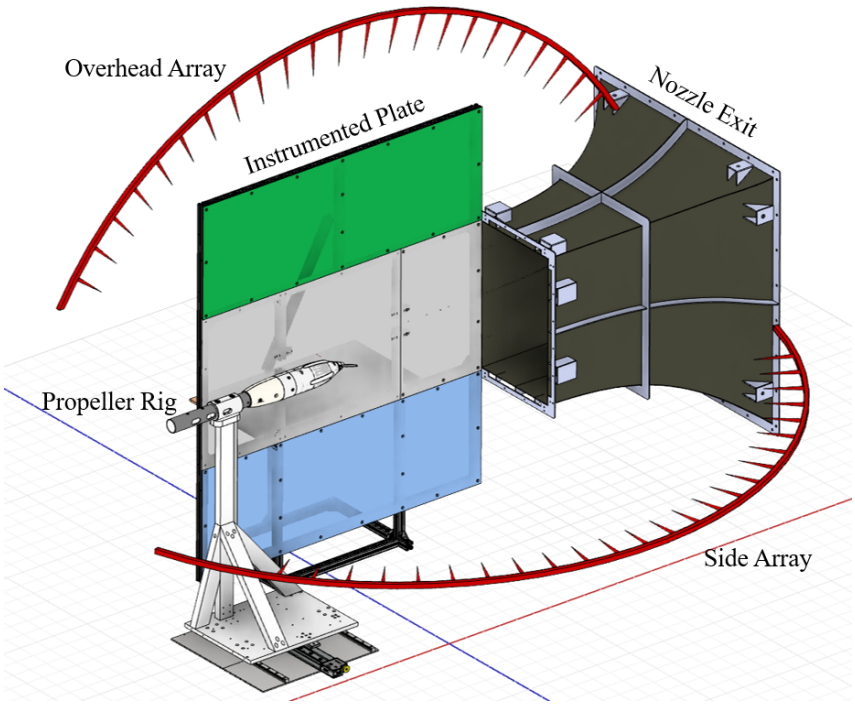

Figure 6: Schematic of the A1 experimental setup at UBRI

The setup depicted in Fig. 6 consisted of a machined aluminium propeller rig mounted adjacent to a heavily instrumented flat plate. A Mejzlik 12x18" two-bladed carbon fibre propeller was used. Three different tripping devices were placed upstream of the propeller to force the development of boundary layers of varying thickness and turbulence levels. The propeller rig housed a load cell and an absolute angular encoder. The propeller rotational speed is closed-loop controlled with a maximum variation of ± 10 RPM.

Far-field acoustics were measured using two far-field microphone arcs placed perpendicular and parallel to the plate, populated with GRAS 40PL microphones. Near-field instrumentation consisted of embedded surface pressure taps and surface pressure transducers (Knowles FG-23329-P07). 2D hotwire anemometry was performed at several locations to obtain flow velocity information.

3.2 Experimental campaign

Three variables were explored: the incoming boundary layer properties, propeller RPM and tip-gap between the propeller and the plate. A constant free-stream velocity of $U = 30$ m/s was used. The acoustic test matrix can be viewed in Table 3. Further details can be viewed in D3.6.

Table 3: Table showing test matrix of acoustic BLI experiments for A1 UBRI (*x,3 mics* means only 3 microphones were connected)

			Instrumentation			
	Conditions		Onboard		Farfield	
Session	**Trips**	**RPMs**	**Encoder**	**Load Cell**	**Overhead Arc**	**Side Arc**
Far-field Acoustics	ABC	Full Sweep			x	x
Near-field Acoustics	ABC	Full Sweep	x		x	x, 3 mics
Load Cell Runs	ABC	Detailed Sweep		x		
Far-field Acoustic Traversed tip gap	ABC	Selection 1	x		x	x
Near-field Acoustic Traversed tip gap	AC	Selection 1	x		x	x, 3 mics
Load Cell Traverse Runs	ABC	6500, 8100		x		

Table 4: Table showing acoustic test matrix of BLI experiments for A1 UBRI (continued)

			Instrumentation	
	Conditions		Nearfield	
Session	**Trips**	**RPMs**	**Surface microphones**	**Static pressure**
Far-field Acoustics	ABC	Full Sweep		
Near-field Acoustics	ABC	Full Sweep	x	x
Load Cell Runs	ABC	Detailed Sweep		
Far-field Acoustic Traversed tip gap	ABC	Selection 1		
Near-field Acoustic Traversed tip gap	AC	Selection 1	x	x
Load Cell Traverse Runs	ABC	6500, 8100		

Table 5: Definition of RPM Selections used in Table 3

RPM sets definition	
Full Sweep	4100:200:8300, 8700, 9000, 9500, 10000
Detailed Sweep	3500:100:4300, 4500:200:8300, 8700, 9000, 9500, 10000
Selection 1	5100, 6500, 8100

3.3 Main results

Key findings were the distinct acoustic signatures observed between the array parallel to the plate (overhead) and the array perpendicular (side). The overhead orientation observed a significant contribution of broadband noise as a result of turbulence ingestion as well as increases in tonal harmonics due to increased unsteady loading on the blades. In contrast, the side array observed minimal broadband noise and consist of mainly tonal contributions.

Additionally, increasing the thickness and turbulence levels of the incoming boundary layer presented significant increases in both tonal and broadband noise in the overhead array, Fig. 7.

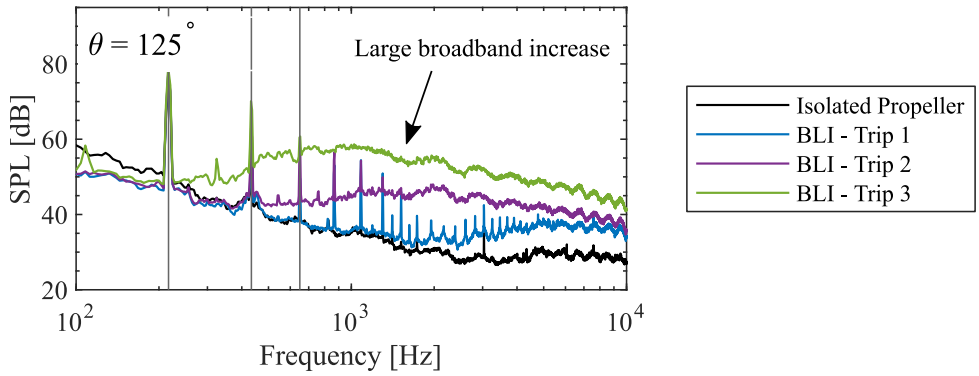

Figure 7: Acoustic SPL spectra varying boundary layer thickness for the $\theta = 125°$ downstream microphone in the overhead array. [6500 RPM, $J = 0.91$, $U = 30$ m/s]

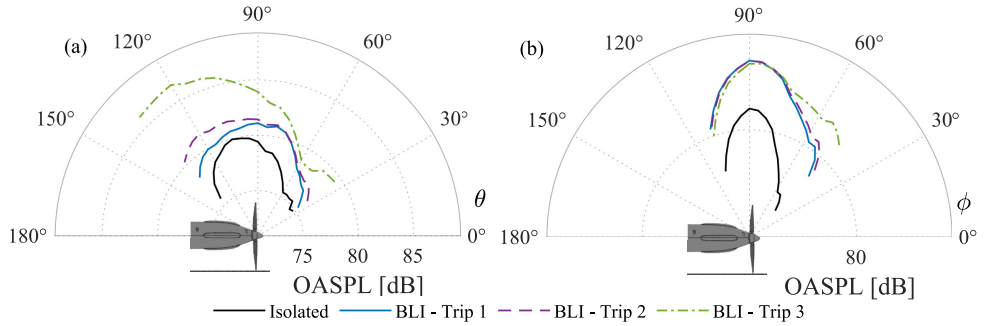

Figure 8: Acoustic directivity patterns for the OASPL noise level measured in the (a) overhead array and (b) side array for varying BL thickness.[6500 RPM, $J = 0.91$, $U = 30$ m/s]

Observations of the Overall Acoustic Sound Pressure Level (OASPL) directivity patterns revealed that the increases were largely focused in the downstream portion of the overhead array, and the upstream portion of the side array (perpendicular to the plate), Fig. 8. This supports the theory that turbulence ingestion noise is predominantly propagated along the blade normals, which corresponds to the downstream portion of the overhead array. Increasing the speed, and hence thrust, of the propeller reduced the separation between the noise levels of the different BLs. Increasing thrust results in a reduced influence of incoming BL properties on the emitted noise. Thus, practical considerations regarding the direction of rotation of the blades and propulsion installation arrangement can be used to customise the profile of the emitted noise signature of a particular BLI implementation.

The ingestion of the boundary layers were seen to have a nearly negligible effect on the propeller thrust and torque, slight increases were seen for thick boundary layers. Full aerodynamic efficiency of the BLI configuration was not able to be performed due to the nature of the setup.

3.4 Main Achievements

A complex experimental test rig was designed and constructed and performed well during the experimental campaign. Development of software to permit synchronous acquisition of data across a diverse set of instrumentation and closed-loop RPM control was achieved and allowed partial automation of the data collection process. Further, a comprehensive dataset was created, processed and documented including necessary velocity profile measurements for simulation initialisation. CAD models of the setup also form part of the Zenodo dataset. The data gathered revealed new information regarding the acoustic properties of a propeller ingesting a planar turbulent boundary layer which can be used to inform preliminary designs of BLI concepts.

3.5 Deliverables

Completed deliverables:

- D3.1: UBRI and UTWE incoming flow and TBL characteristics
- D3.3: Configuration A experimental databases (without mitigation)
- D3.6: Documentation of experimental databases (without mitigation)
- D3.7: WP3 final public report [This document]

3.6 Dissemination

In addition to the publication of the dataset (`https://doi.org/10.5281/zenodo.7924655`) and deliverables, two AIAA23 AVIATION Conference papers were published using the data from this campaign:

Zaman, I., Falsi, M., Zang, B., Azarpeyvand, M., & Camussi, R. (2023). Experimental Parametric Investigation of the Haystacking Phenomenon for Propeller Boundary Layer Ingestion. In AIAA AVIATION 2023 Forum (p. 4054).

Zaman, I., Falsi, M., Zang, B., Azarpeyvand, M., & Camussi, R. (2023). Effect of Tip Gap on Nearfield and Farfield Acoustics of Propeller Boundary Layer Ingestion. In AIAA AVIATION 2023 Forum (p. 4055).

4 Configuration A2

4.1 Experimental Setup

Similar to the A1-UBRI experiment, the objectives of the A2 configuration constituted the generation of a comprehensive experimental dataset in the Aeroacoustic Facility at UBRI using a purpose-built experimental setup. The data would contain far-field acoustic data, near-field surface pressure, propeller forces, flow velocity surveys and synchronised blade position information across a wide range of operational parameters.

This data would then be used to draw inferences into the acoustic properties of BLI of an APG boundary layer and serve as inputs to the numerical partners. Portions of the dataset are to be published. Full details of the experimental setup and instrumentation used at UBRI for this campaign can be found in D3.6 and D3.3. A brief overview will be given here.

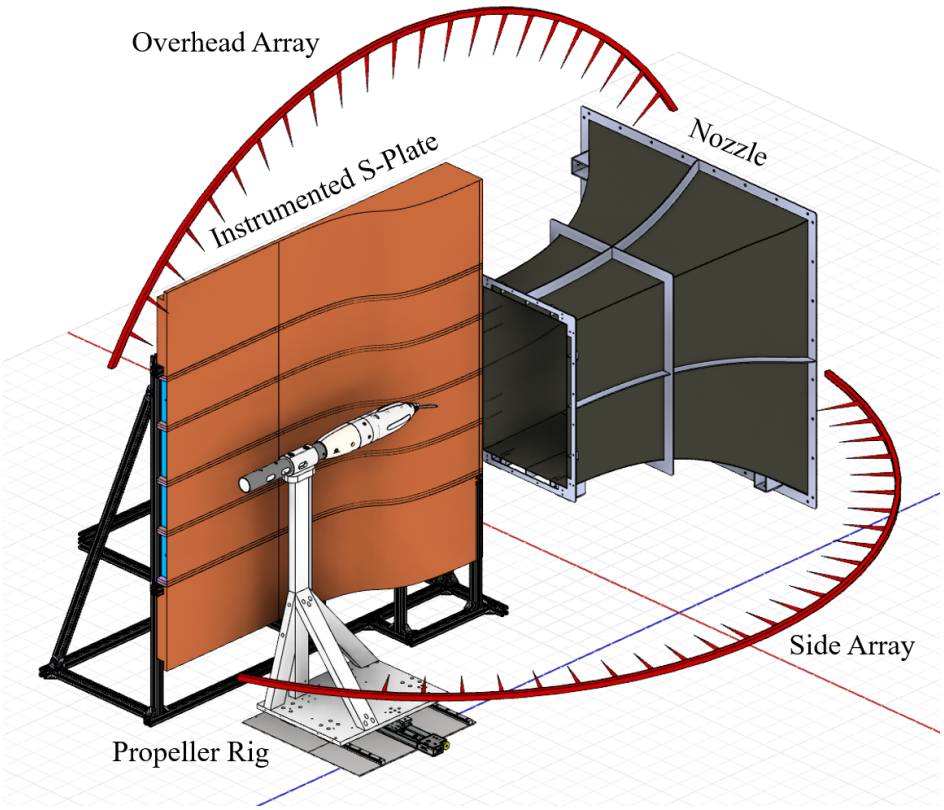

Figure 9: Schematic of the A2 experimental setup at UBRI

The setup depicted in Fig. 9 consisted of a machined aluminium propeller rig mounted adjacent to an instrumented S-plate. The curved section of the S-Plate was defined using a cubic bezier function. A Mejzlik 12x18" two-bladed carbon fibre propeller was used. An 90-grit sandpaper trip was placed at the nozzle exit to initialise the flow. The propeller rig housed a load cell and an absolute angular encoder. The propeller rotational speed is closed-loop controlled with a maximum variation of ± 10 RPM.

Far-field acoustics were measured using two far-field microphone arcs placed perpendicular and parallel to the plate, populated with GRAS 40PL microphones. Near-field instrumentation consisted of embedded surface pressure taps and surface pressure transducers (Knowles FG-23329-P07). 2D hotwire anemometry was performed at several locations to obtain flow velocity information.

4.2 Experimental campaigns

Three variables were explored: the propeller RPM, tip-gap between the propeller and the plate, and the streamwise position of the propeller along the curve. Two freestream velocities were used. The acoustic test matrix can be viewed in Table 6. Further details, including the hotwire velocity survey, can be viewed in D3.6.

Table 6: Table showing the acoustic test matrix for configuration A2

Type	RPM Sweep		Tip Traverse	
Session	Acoustic	Performance	Acoustic	Performance
Propeller Position, X [cm]	48, 80, 100	48, 80, 100	48, 80	48, 80
U_{inf} [m/s]	27, 25	27, 25	27	27
RPM	Full Sweep	Detailed Sweep	Selection 2	Selection 2
Instrumentation				
Encoder	x	x	x	x
Load Cell		x		x
Overhead Arc	x		x	
Side Arc	x		x	
Surface microphones	x		x	
Static pressure	x		x	

Table 7: Table showing the definitions of the RPM sets seen in Table 6 for the A2 configuration

RPM sets definition	
Full Sweep	5100:200:8300, 8700, 9000, 9500, 10000
Detailed Sweep	3500:100:4300, 4500:200:8300, 8700, 9000, 9500, 10000
Selection 2	6500, 8100

4.3 Main results

It was first determined that the S-Plate did indeed generate a strong adverse pressure gradient boundary layer over its surface, seen in Fig. 10. Hotwire velocity surveys also showed a clear separation region, Fig. 11. It was also observed that the level of turbulence in the boundary layer far exceeded that of the A1 flat plate. This resulted in strongly increased acoustic emissions. Directivity patterns at low RPM exhibited a similar pattern to that of the A1 configuration, with noise directed in the downstream direction, at higher RPM, the pattern adopts a more even distribution. A key result is the strong presence of acoustic haystacking in the spectra, the phenomenon whereby the broadband noise emission correlate to form humps at slightly above the BPF (Blade Passing Frequency) harmonics.

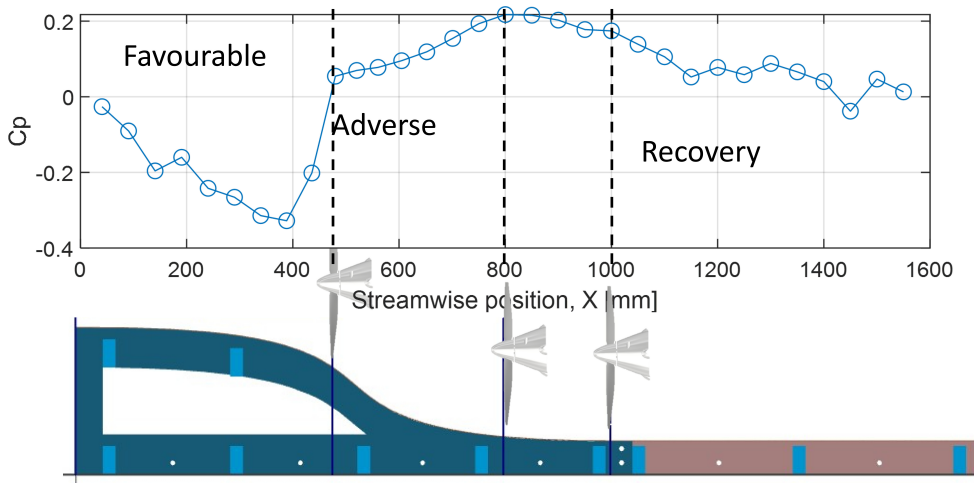

Figure 10: Static pressure coefficient, Cp, streamwise distribution over the S-Plate without propeller. Showing presence of advers pressure gradient. [$U = 27$ m/s]

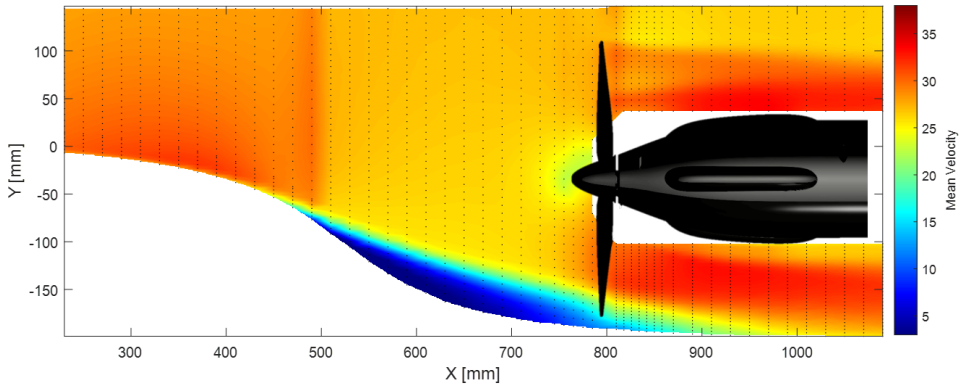

Figure 11: Mean velocity contour plot, using traversing hotwire probes. [$U = 27$ m/s, 7500 RPM]

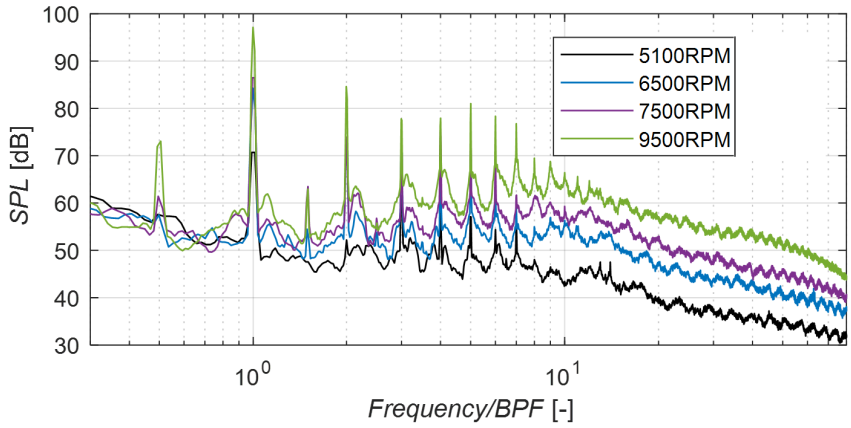

Figure 12: Acoustic spectra measured at the $\theta = 90°$ microphone for increasing RPM showing significant haystacking of the broadband noise around the BPF harmonics. [$U = 27$ m/s]

Varying the streamwise position of the propeller was seen to have great effect on the emitted noise

signature, with upstream positions where the turbulent content of the BL was much lower due to thinning of the BL at the beginning of the curve, emitting significantly lower noise levels, Fig. 13

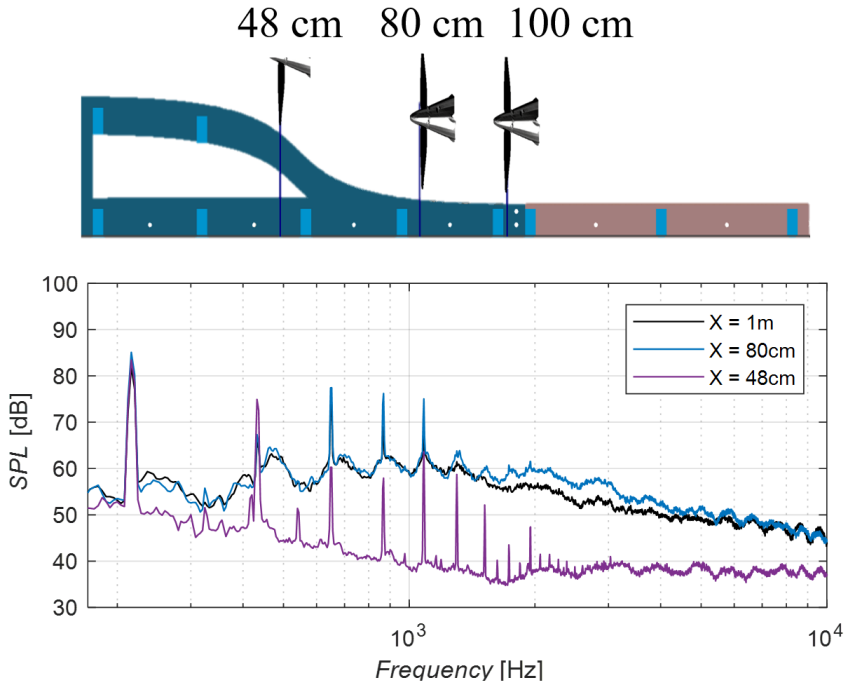

Figure 13: Acoustic spectra measured at the $\theta = 120°$ microphone for different rotor streamwise positions . [$U = 27$ m/, 6500 RPM]

4.4 Main Achievements

A complex experimental test rig was designed and constructed and performed well during the experimental campaign. Including the instrumented curved plate. Development of software to permit synchronous acquisition of data across a diverse set of instrumentation and closed-loop RPM control was achieved and allowed partial automation of the data collection process. Further, a comprehensive dataset was created, processed and documented including necessary velocity profile measurements for simulation initialisation. CAD models of the setup also form part of the Zenodo dataset. The data gathered revealed new information regarding the acoustic properties of a propeller ingesting an adverse pressure gradient turbulent boundary layer which can be used to inform preliminary designs of partially embedded BLI concepts.

4.5 Deliverables

Completed deliverables:

- D3.3: Configuration A experimental databases (without mitigation)
- D3.6: Documentation of experimental databases (without mitigation)
- D3.7: WP3 final public report [This document]

4.6 Dissemination

The documented Zenodo dataset is published at: `https://doi.org/10.5281/zenodo.7924655`.

5 Configuration B1

This section provides a detailed overview of the experimental setup and findings for configuration B1, which focuses on analyzing the aerodynamic and acoustic interactions in a system consisting of distributed propellers installed side-by-side and upstream of a wing. The report presents the experimental campaigns conducted, the measurement techniques employed, and the main results obtained. It highlights the impact of synchrophasing on slipstream characteristics, acoustic emissions, and slipstream deformation. The section concludes with the main achievements and deliverables of the study. The data and analysis presented in this report contribute to a better understanding of the aerodynamic and acoustic behavior of distributed propeller configurations.

5.1 Experimental Setup

The experimental setups were composed of three six-bladed propellers made of steel. These propellers, named XPROP-S, had a radius of $R = 101.6$mm. Additionally, a fourth mirrored propeller was used to mimic a counter-rotating configuration by inverting the rotation direction of the middle propeller. In the first set of experiments, the propellers were arranged side by side and connected to an aluminum nacelle, which was then attached to a support sting. The support sting had a NACA 0020 profile with a chord of $c = 100$mm (with the last two millimeters truncated due to manufacturing capability). In the second set of experiments, the propellers were connected to the nacelle, and each nacelle was mounted on an unswept, untapered wing model featuring an NLF-Mod22(B) airfoil. The wing had a chord of 0.3m and a span of 1.248m. The propellers were powered by brushless DC electric motors enclosed in the nacelle. Each motor was controlled by a dedicated PWM-controlled trapezoidal electronic speed controller (ESC) and a programmable 5kW DC power supply. The motors were angled downwards at a 5° angle relative to the wing's chord.



Figure 14: Upstream view of the LTT test sections with setups of the first (left) and second (right) experimental campaign.

5.2 Experimental campaigns

The experiments were conducted at the Low-Speed, Low-Turbulence Tunnel (LTT) located at Delft University of Technology (TUD). This wind tunnel is a closed-circuit type with a maximum freestream velocity of $120\,\mathrm{m\,s^{-1}}$ and turbulence levels below 0.04% for the freestream velocity used in the experiments ($V_\infty = 30\,\mathrm{m\,s^{-1}}$). Its test sections have an octagonal cross-section with dimensions of 1.25m in height, 1.8m in width, and 2.6m in length. For the acoustic measurements, a specially designed acoustic test section with lined side panels and a recessed microphone array from a Kevlar panel was used. Additionally, the floor and ceiling of this acoustic test section were covered with 3cm thick Basotect melamine foam to minimize acoustic reflections.

The primary focus of the first experiment was to investigate the impact of synchrophasing on slipstream characteristics within a time-averaged framework. Specifically, the study examined the co-rotating configuration. To analyze the synchrophasing, the relative blade-phase angle ($\Delta\phi$) was varied from 0° to

50° in increments of 10°. In the random case, the rotational speeds of the outer propellers were increased by 0.03Hz compared to the middle propeller. This speed difference allowed the relative blade-phase angle to cover approximately one blade passage (0° to 60°) during each measurement point and had a negligible effect on the propeller's performance. The shaft incidence angle was set at $i = 0°$, and the tip clearance is $d = 0.04R$. The flow characteristics within the slipstreams were measured using a five-hole probe. Additionally, a pitot tube was installed on the test section wall upstream of the model to capture the total and static pressures. The pressure measurements have an estimated uncertainty of ±4Pa, and one axis and three planes were investigated. The test conditions parameters are summarized in Table 8.

Parameter	Evaluated values	Baseline value
Freestream velocity V_∞ [m/s]	30	30
Blade pitch *beta* at $r/R = 0.7$ [deg]	30	30
Advance ratio J	0.80, 1.00, 1.35	1.00
Relative blade-phase angle $\Delta\phi$ [deg]	random, 0, 10, 20, 30, 40, 50	random
Rotation direction	co-rotating	co-rotating
Incidence angle i [deg]	0	0
Tip clearance d/R [-]	0.04	0.04

Table 8: Test conditions of the first experimental campaign of configuration B1.

In the second experiment, the three propellers were installed on the leading edge of a wing. This experiment aimed to investigate the impact of synchrophasing on the acoustic emissions of a distributed propeller system in a tractor configuration, as well as analyze the deformation of the combined slipstream as it passes by a wing installed downstream. The electric motor limited the propellers to an advance ratio of $J = 0.8$ (184.5Hz), but measurements were also performed at $J = 1.0$ (147.6Hz). The relative blade angles ranged from 0° to 50° in 10-degree intervals. The tip clearance between propellers was approximately 5% of the propeller radius. To simulate a counter-rotating configuration, the middle propeller was replaced with a mirrored version of the original propeller. The wing's angle of attack varied from 0° to 10°. Measurements were obtained using a single propeller mounted on one of the three nacelles to differentiate between interactions with adjacent propellers and interactions with adjacent nacelles. However, isolated configurations with only one propeller and no adjacent nacelles were not tested due to time constraints. An overview of the test conditions can be found in Table 9.

Table 9: Test conditions and configurations of the second experimental campaign of configuration B1.

Parameter	Evaluated values	Baseline value
Freestream velocity V_∞ [m/s]	30	30
Blade pitch β at $r/R = 0.7$ [deg]	30	30
Advance ratio J [-]	0.80, 1.0	0.80
Relative blade-phase angle $\Delta\phi$ [deg]	random, 0, 10, 20, 30, 40, 50	random
Rotation direction	co-rotating, counter-rotating	co-rotating
Tip clearance d/R [-]	0.05	0.05
Angle of attack of the wing AoA [deg]	0, 2, 5, 8, 10	2
(P)propeller/(N)acelle configuration	3P + 3N, 1P + 3N	3P + 3N

Three types of measurement techniques were employed to gather data on the system's noise, wing surface pressure, and slipstream deformation. Acoustic measurements were conducted using a phased microphone array consisting of 64 microphones. The elliptical array extended 1.6m in the streamwise direction and 0.4m vertically, with the microphones recessed from the Kevlar side wall and held by a solid plate lined with melamine foam. Each measurement lasted 30s with a sampling frequency of 51.2kHz. Wing surface pressure was recorded using pressure taps. Two rows of pressure taps were placed at $0.7R$ from the centerline of the middle propeller in the chordwise direction. An electronic pressure scanner with a sampling frequency of 10Hz simultaneously measured all taps for a duration of 5s. To capture

slipstream deformation downstream of the setup, a wake rake equipped with total and static pressure probes was utilized. The wake rake was positioned one chord-length from the wing trailing edge, aligned with the middle propeller. It traversed vertically in 10mm increments. The pressure ports of the wake rake were connected to the same electronic pressure scanner used for the previous measurement. It is important to note that the wake rake and its support rig were exclusively used during the slipstream measurements and were not present in the tunnel during the acoustic measurements.

5.3 Main results

The first campaign revealed that at an advance ratio of $J = 1.00$, the adjacent slipstreams do not merge within the examined spatial limits, particularly for distances less than $1.4R$ downstream from the propeller disks. The relative blade-phase angle not only affects the width of the gap between the slipstreams but also its position, either moving inward or outward based on the syncrophasing angle. Regardless of the cases investigated, including the random one, there always exists a gap between the slipstreams, with its length and position along the Y-axis determined by the relative blade phase angle. The smallest length, corresponding to the maximum widening of the adjacent slipstreams, is observed at $\Delta\phi = 0°$ (Figure 15, left), while the largest length occurs at $\Delta\phi = 30°$ (Figure 15, right), resulting in almost double the size of the gap at $X = 1.4R$. In terms of the gap position along the Y-axis, a maximum outward translation is observed at $\Delta\phi = 10°$, leading to the widest middle slipstream, while the side slipstream experiences negligible changes compared to the slipstream of an isolated propeller. Conversely, at $\Delta\phi = 50°$, the opposite occurs (Figure 16).

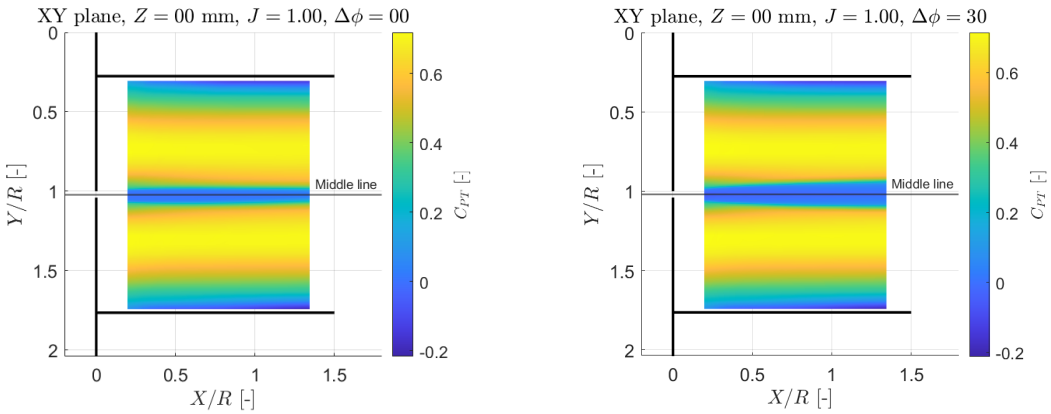

Figure 15: Gap width along the Y-axis between slipstreams.

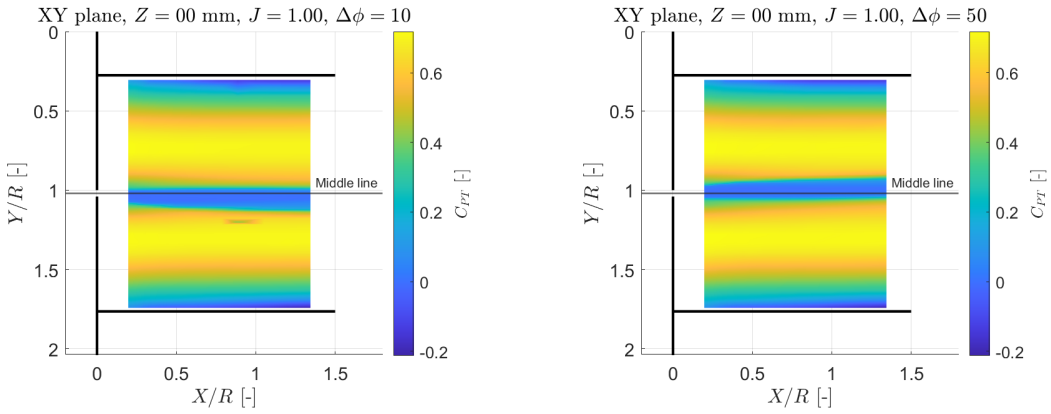

Figure 16: Slipstreams gap translation along the Y-axis.

In the second experimental campaign, several mean results were obtained for the array + wing configuration. It was observed that the relative blade phase angle has a significant impact on the acoustic of the system, with differences within 10dB in a specific location. Furthermore, differences of up to 14dB were observed between the suction and pressure sides (Figure 17). The total-pressure distribution in the wake was found to be dependent on the relative phase angle of the propellers. Additionally, the wing angle of attack was found to have a significant impact on the slipstream deformation, particularly in the lower half of the wing (Figure 18).

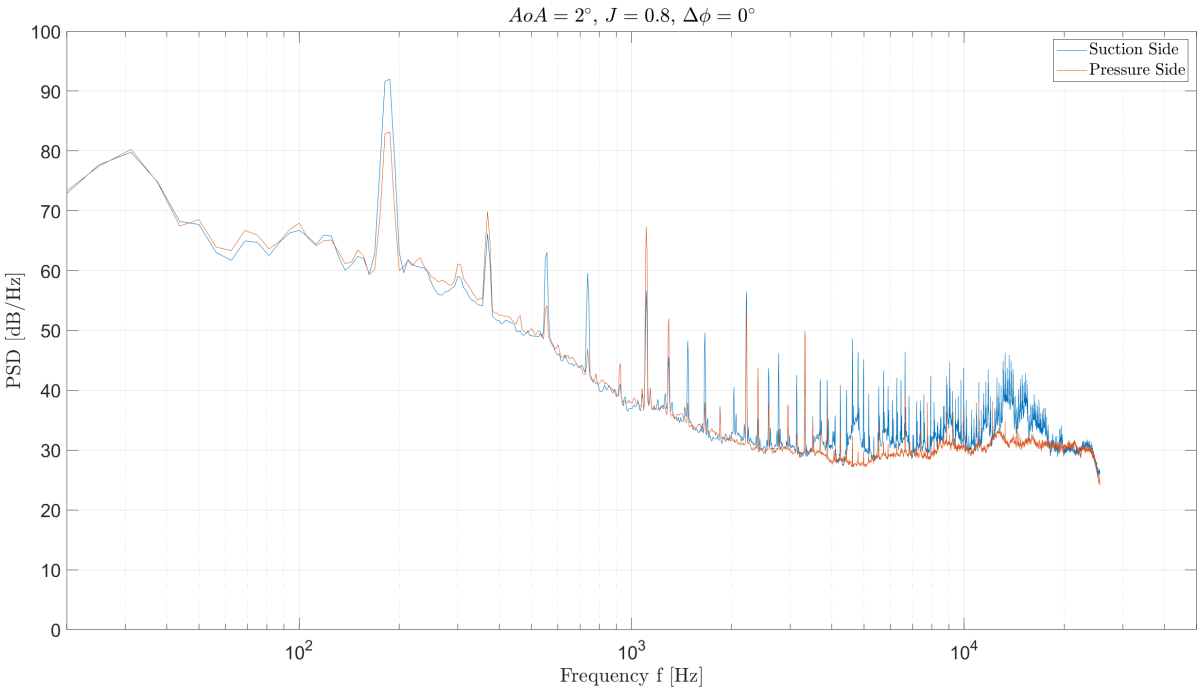

Figure 17: Noise power spectral density (PSD) differences between pressure and suction sides for microphone located in the middle of the microphone array.

5.4 Main Achievements

A sophisticated experimental test rig was designed and built to collect essential data for configuration B1. Initially, aerodynamic measurements were conducted with a semi-B1 setup, consisting solely of the propeller array. Subsequently, both aerodynamic and acoustic measurements were carried out in an experimental configuration that included a wing installed downstream. This comprehensive investigation yielded valuable insights into the effects of synchrophasing. The resulting dataset was meticulously processed, documented, and supplemented with CAD models of the setup, all of which can be found in the Zenodo dataset. The gathered data uncovered novel information about the acoustic and aerodynamic characteristics of a configuration featuring multiple propellers installed at the leading edge of a wing.

5.5 Deliverables

The data obtained from the experimental campaigns and the subsequent analyses have been described in deliverables D3.2, D3.4, D3.6, and D3.7.

5.6 Dissemination

- Monteiro, F. do N., Ragni, D., Avallone, F., Sinnige T., "Low-order acoustic prediction tool for estimating noise emissions from distributed propeller configurations", AIAA Aviation 2023 Forum,

San Diego, 12-16 June 2023. (TUD) DOI: https://doi.org/10.2514/6.2023-4180

- Fernanda do Nascimento Monteiro, Daniele Ragni, Tomas Sinnige, Francesco Avallone. (2023). H2020 ENODISE: TUD Experimental database configuration B1 (v1.0) [Data set]. Zenodo. https://doi.org/10.5281/zenodo.8307371

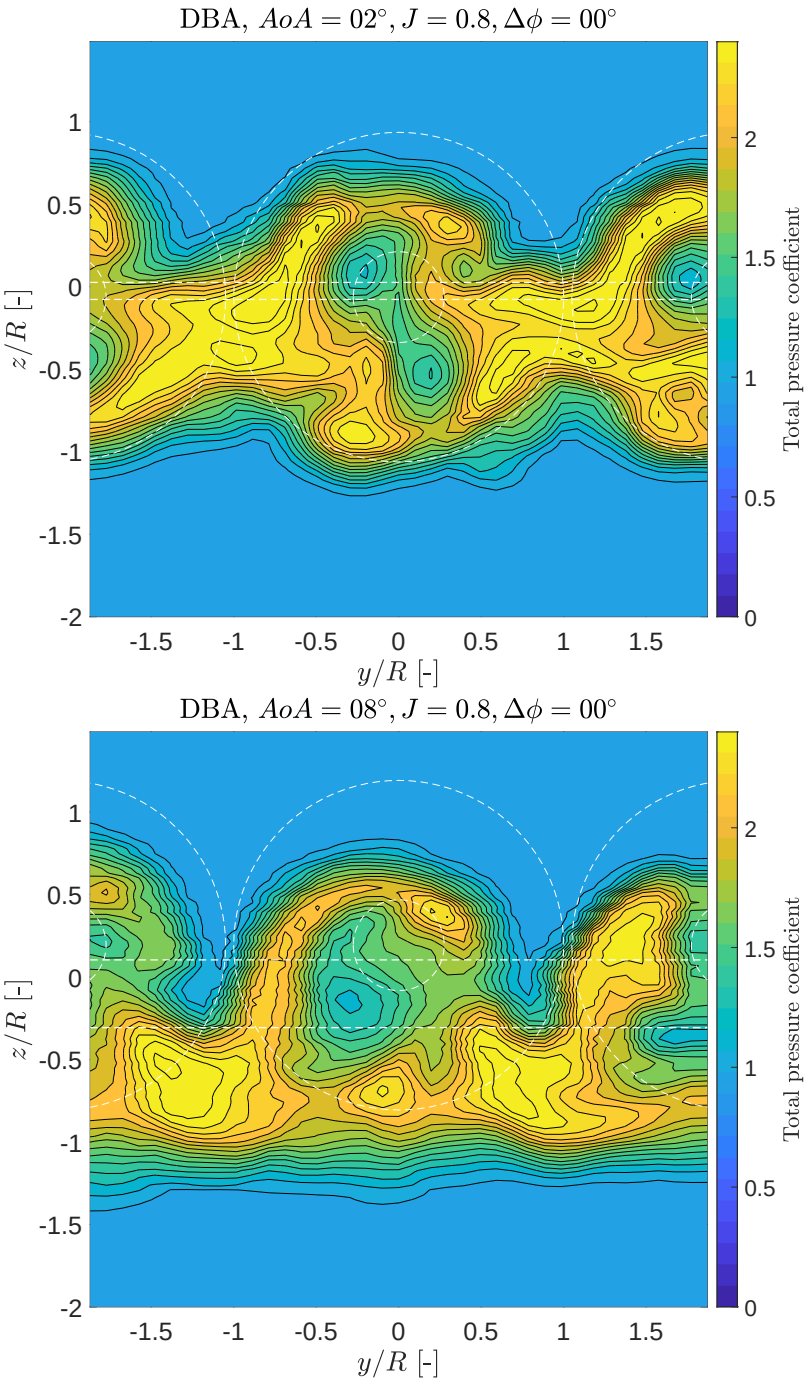

Figure 18: Wing angle of attack impact on the slipstream deformation.

6 Configuration B2

6.1 Experimental Setup

The ECL experiment is primarily dealing with the scattering of propeller noise by a wing, for an over-the-wing installation and a pair of side-by-side propellers as shown in Figure 19. The experiment is aimed at demonstrating the feasibility of determining an optimum configuration in terms of sound masking by the wing, with regards to observers located below the wing, preserving acceptable aerodynamic performances. Therefore, both the aerodynamic noise and the performances in terms of combined wing lift and propeller thrust must be considered as parameters for the optimization. Several configurations were experimentally assessed, regarding the five parameters shown in Figure 20 and listed in Table Table 10.

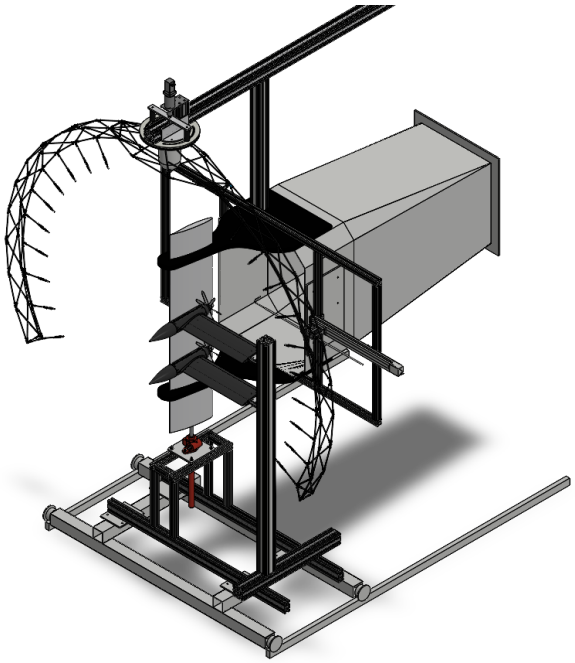

Figure 19: CAD view of the full setup.

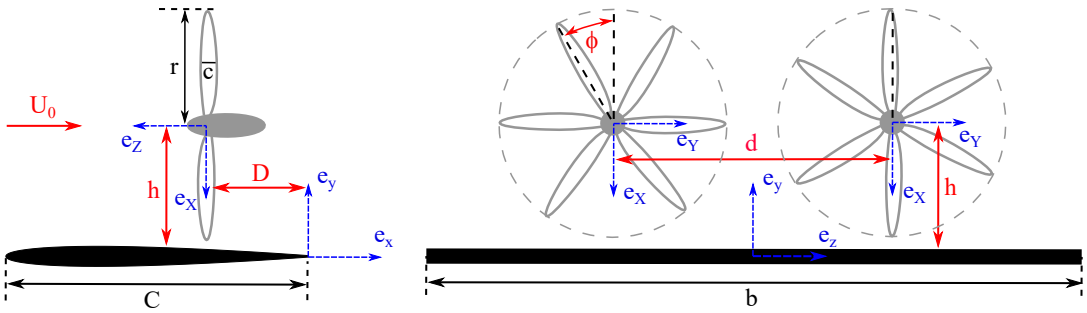

(a) Side view (b) Front view

Figure 20: Schematics of the propellers-wing arrangement, reference frames, and main notations.

Realistic enough features must be included in the experiment, in order that the search for an optimum makes sense. For this, the two propellers are synchronized, with adjustable phasing in terms of the relative angular positions of the blades. They can be either corotating or contrarotating. Furthermore, the wing-body is a rectangular airfoil, extruded from the cross-section of a true lifting wing of aircraft, namely the

Table 10: Setup parametric variations.

	1	2	3
D	0.1r (0.01m)	0.5r (0.05m)	r (0.1m)
h	r+0.1r (0.11m)	r+0.5r (0.15m)	-
d	2r+0.1r (0.21m)	2r+0.5r (0.25m)	-
ϕ	0°	30°	-
U	0 m/s	22 m/s	-

F15 shape, with courtesy of DLR. The vertically mounted scattering unswept wing [2] has 0.3 m chord, and 1.4 m total span, for a wetted span of 0.9 m. Additionally, it is set to a non-zero lift angle of attack, kept unchanged in the experiment. The 6-bladed "XPROP-S" propellers from TUD [3, 4], with about 0.2 m diameter and $\gamma = 30°$ blade pitch angle are installed at different positions near the trailing edge, with adjustable separation.

Even though several configurations were experimentally assessed and analyzed, as described in Table 10, only the most critical cases i.e., configurations with maximum (Max) and minimum (Min) D, h, and, d parameters are discussed for both offset phase angles ϕ as shown in Figure 21.

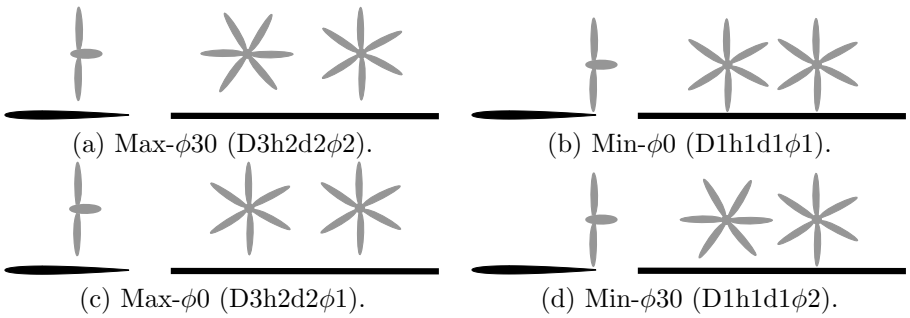

(a) Max-ϕ30 (D3h2d2ϕ2). (b) Min-ϕ0 (D1h1d1ϕ1).

(c) Max-ϕ0 (D3h2d2ϕ1). (d) Min-ϕ30 (D1h1d1ϕ2).

Figure 21: Critical tested configurations.

6.2 Experimental campaigns

Experiments are performed in the open-jet high-speed anechoic wind tunnel in the Fluid Mechanics and Acoustics Laboratory (LMFA) of *École Centrale de Lyon* (ECL) [5]. The nozzle dedicated to the project has an exit cross-section of 0.9 m height and 0.7 m width, with 'vignetted' corners. It issues in an anechoic chamber, with average length, height, and width of 10 m, 9 m, and 8 m, respectively.

The selected wind tunnel speed for the experimental campaigns was 22 m/s, corresponding to a Reynolds number of 4.5×10^5, based on the chord length of the model wing. Tests were performed for different model configurations, varying the position of the propellers but maintaining the propellers' direction, and RPM settings. The incident flow was always aligned with the propeller axis. Prior to these tests, a reference configuration has been defined, as a clean configuration with no propellers. For this, the wing was also tested for a single deflection angle $\alpha = 10°$.

Acoustic measurements were carried out with an array of 20 Bruel & Kjaer type 4958 1/4" free-field microphones, distributed around the model on a rotating arc antenna of 2 m diameter, as shown in Figure 22. The antenna rotates around the vertical axis to cover a portion of a sphere and obtain three-dimensional sound-directivity patterns. The axis coincides with the trailing edge of the wing.

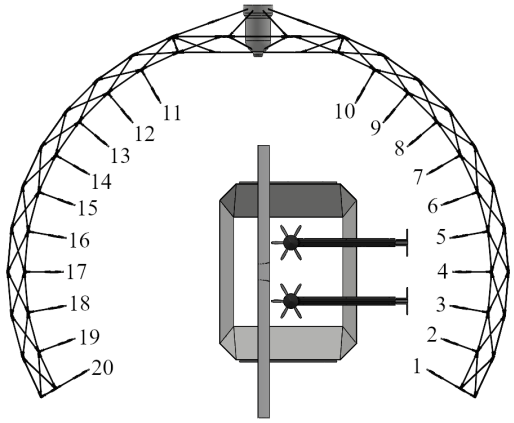

Figure 22: Antenna location regarding the wing-propellers system and microphone numbering. The antenna axis coincides with the wing trailing edge. Antenna set at 0° angle.

The wing model instrumentation includes two chordwise sets of 32 steady-state pressure taps distributed on both pressure and suction sides, with refined distributions close to the LE and in the aft part on the suction side, where the propellers are positioned.

The propeller torque moments, as well as tension and compression loads, were measured with a Futek MBA500 (100/100) Bi-Axial Load Cell.

6.3 Main results

6.3.1 Aerodynamic Performances

Figure 23 presents a summary of the lift-coefficient C_L results computed from the C_P of each tested configuration. What stands out in this figure, is the higher influence of the h parameter (the distance from the tip of the blades to the wing) on C_L. Among all configurations, this is a key parameter. The lift also increases when the rotation of the propellers is synchronized with zero angular offset ($\phi = 0$), while the distance between them (d parameter) has a slight effect. In fact, for all the configurations, the C_L is less than 3% lower for the cases of $d2$. Finally, the D parameter also has an important role. The closer the blades approach the TE, the higher the lift increases, with a steeper slope for the $h1$ configurations.

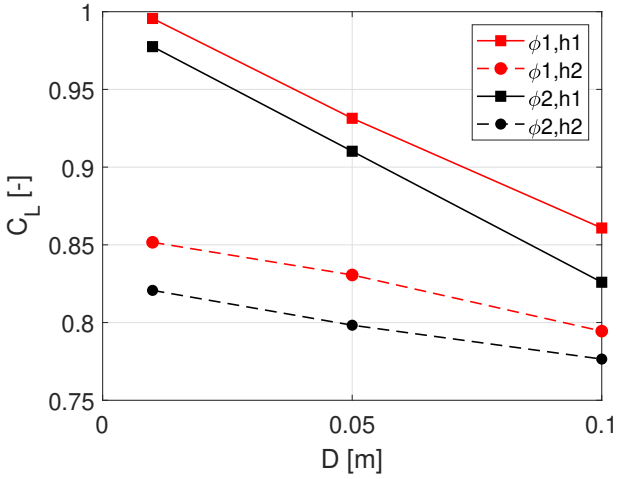

Figure 23: Effect of different parameters on the C_L with $d1$

As can be seen in Figure 24(a), an almost homogenous Cp in the spanwise direction is achieved with the Max-ϕ30 configuration, in both the pressure and suction sides and the maximum C_P peak (being the no propellers case the perfect homogeneity). By contrast, Figure 24(b) exhibits a different behavior with spanwise heterogeneity along the measured wing suction side with the Min-ϕ0 configuration. An increase in the C_P close to the TE and upstream of the plane of the propellers is easily identified, in the form of a hump. This effect is generated by the induced velocity of the propellers, which causes a decrease in the pressure over the wing surface. The hump suddenly decreases close to the tip of one of the propellers, where the induced flow interacts with the surface of the wing (this depends on the direction of rotation).

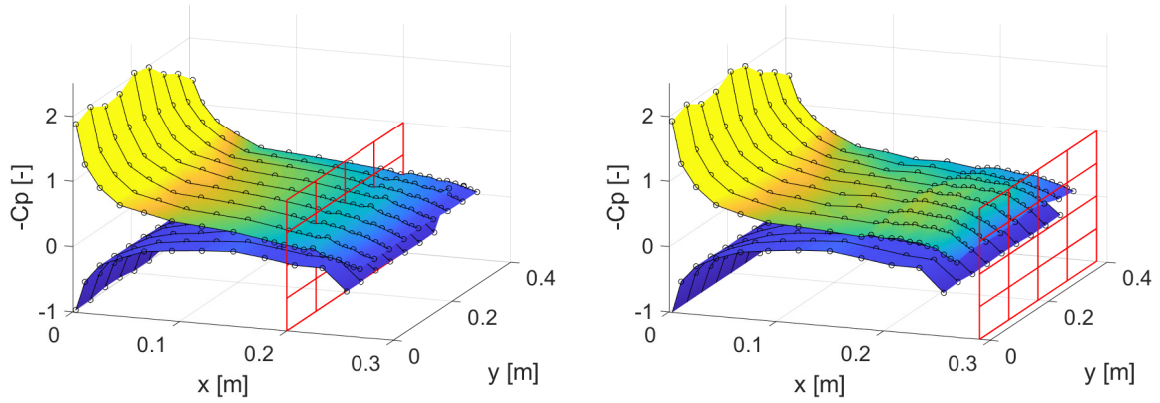

(a) Max-ϕ30 (b) Min-ϕ0

Figure 24: 3D C_P plots. In red is shown the plane of the propellers.

6.3.2 Far-Field Sound Inspection

The effect of the five selected parameters on the OASPL is depicted in Figure 25(a,b) for microphones 4 and 17 and for the 90° antenna position (which would correspond to observers above and below the wing, respectively, case of Figure 22). Frequencies below 100 Hz are ignored in the calculation of the OASPL, as attributed to the background noise. As expected, the noise levels are $3-5$ dB higher for Mic 4 than for Mic 17 in all configurations, due to scattering by the wing, even for configurations where propellers are close to the TE. Even though the results are not far from each other when comparing one specific microphone, differences and trends can still be identified, especially for the D parameter that makes configurations noisier as propellers approach the TE. The parameter ϕ appears to have a critical effect on the measured OASPL. For all the configurations, the noise is obviously higher when propellers are synchronized with a phase of 30°. The plots show that the d parameter is sensible as well, the less the gap between the blades, the higher the noise. Finally, the distance h between the wing and the blades is not as important as the previous parameters. Nevertheless, the system is around 5% less noisy when that distance is large. Clearly, bigger differences can be found depending on the microphone and antenna position selected, as will be shown later in the 3D results.

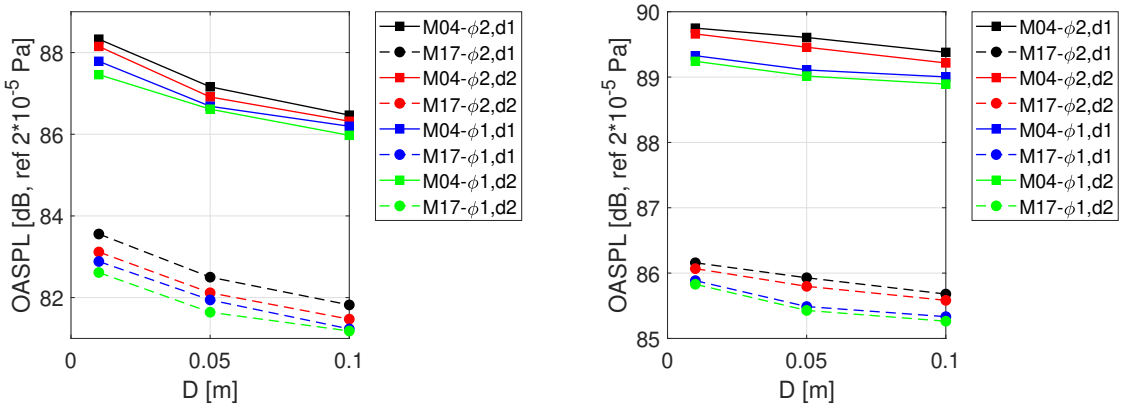

(a) Flow case ($J = 0.95$) (b) No-flow case ($J = 0$)

Figure 25: Effect of D, ϕ, d parameters on the propellers OASPL ($0.1 - 24\ kHz$) with $h1$. M04 = mic. 4, M17 = mic. 17.

The masking effect produced by the wing is highlighted in Figure 26, for both Min-ϕ30 and Max-ϕ0 configurations, in the high-frequency range, where the sound level for the mic. 17 (below the wing) is less noisy by at least $5 - 10\ dB$.

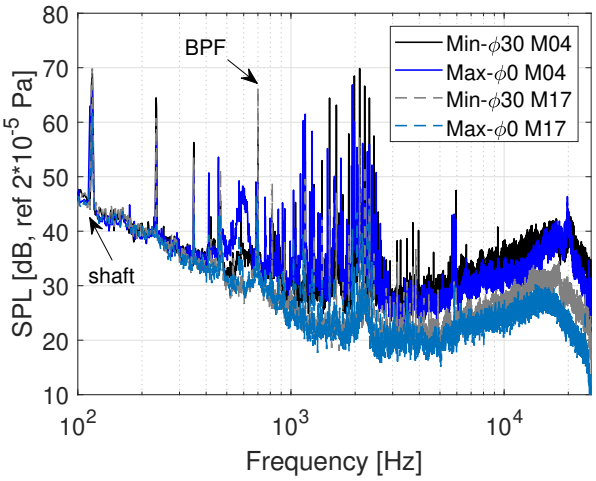

Figure 26: Evidence of masking effect in louder and quieter configurations with $J = 0.95$.

Comparing results in Min-ϕ30 configuration with and without the wing in Figure 27(a,b), shows that for both portions of the sphere, sound at the BPF significantly increases in the presence of the wing, because of sound reflection and regeneration for the microphones located over and under the wing, respectively. In both cases, the sound is also higher for microphones 5 to 9 which are shifted in the direction of rotation of the propellers, as well as for a symmetrical area on the opposite side. This tends to feature a dipole-like pattern with an axis to the direction of rotation. Configuration Min-ϕ30 is typical of a significant amplification by installation effect, because of the close vicinity of the blade tips to the trailing edge of the wing. The same tilting effect of the dominant directivity lobe seems to be also evidenced in all configurations. Large differences are also found between Min-ϕ30 and Max-ϕ0, the loudest and quietest configurations with flow, respectively. Figure 27(c) illustrates a general fact: the larger the distance between the propellers and the wing (from the surface and from the trailing edge), specifically for $\phi = 0$, the lower the tonal noise, for both sides above and below the wing. Changing the

ϕ parameter between Max-ϕ0 and Max-ϕ30 produces significant changes (Figure 27(d)).

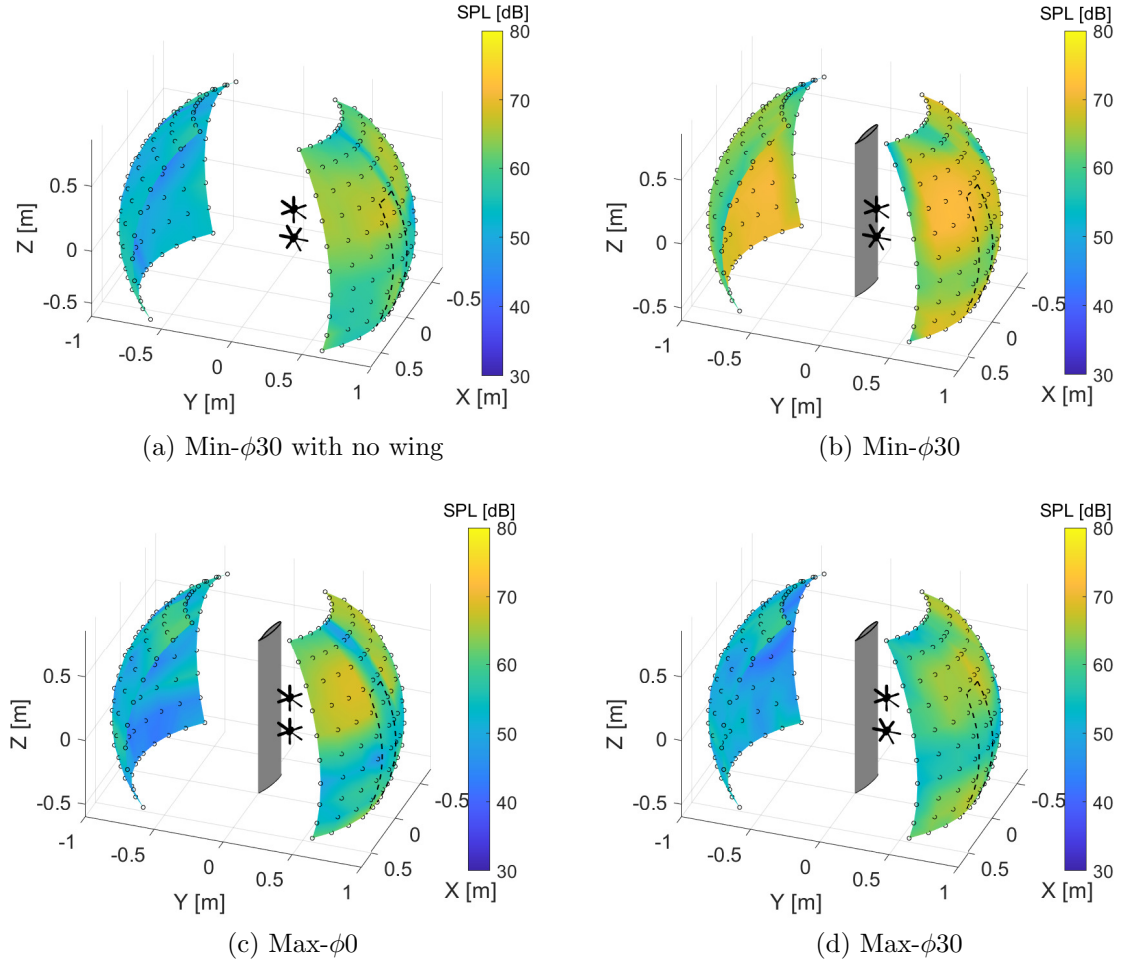

(a) Min-ϕ30 with no wing

(b) Min-ϕ30

(c) Max-ϕ0

(d) Max-ϕ30

Figure 27: Compared 3D directivity patterns of the 1st BPF (700 Hz) in various configurations.

6.4 Main Achievements

Different parameters have been found to produce dominant effects on various aerodynamic or acoustic quantities, important for the identification of either detrimental or beneficial configurations. The streamwise distance D from the propeller plane to the TE is the only common critical parameter, for both aerodynamic performances and noise. The normal distance from the propeller axis to the wing surface h mainly affects the wing C_p distribution and lift. The axis-to-axis distance d between the propellers mainly affects their thrust, whereas their relative phase angle ϕ has a significant effect on the far-field sound. It is important to state that the best configuration regarding the aerodynamic performances is detrimental to the acoustic signature, and *vice versa*. In particular, sound radiation is strongly increased when the blade tips operate close to the trailing edge; in the same conditions, both the wing lift and propeller thrust reach their maximum, for fixed advance ratio and rotational speed. More quantitatively, depending on the positions of the propellers, the lift coefficient of the wing can be increased by up to 30%, compared to the wing-alone configuration, and the thrust of the propellers can be up to 45% higher than in the case of only one propeller without the wing. Sound reductions, mainly by masking, of up to 5 dB in the overall sound pressure level and 20 dB at the blade passing frequency, were observed. The results also indicate that the installation effect is very crucial for tonal propeller noise, leading to either masking or regeneration of sound for noise exposure on the ground, depending on propeller positions

above the wing. This high sensitivity to the parameters confirms that the present experiment is relevant for the parametric investigation.

The study was primarily aimed at producing a database, usable for finding an optimum configuration, rather than directly proposing an optimum. Indeed, the definition of the latter is a multi-disciplinary end-user task, for which criteria must be defined, leading to some relevant aeroacoustic cost function. The database is also now available for the validation of analytical and/or numerical prediction strategies.

6.5 Deliverables

3.2, 3.4, 3.6, and 3.7.

6.6 Dissemination

- Acevedo-Giraldo, D., Roger, M., Jacob, M. C., & Beriot, H. (2022). Analytical study of the aerodynamic noise emitted by distributed electric propulsion systems. In 28th AIAA/CEAS Aeroacoustics Conference 2022 (p. 2830).
  `https://doi.org/10.2514/6.2022-2830`

7 Configuration B3-VTOL

Configuration B3 concerns a conceptual flap-mounted propulsion system intended for vertical take-off. This configuration has been divided into two sub-configurations, B3-VTOL and B3-Flap. In this section, an overview of the experiments and main results for B3-VTOL is presented. The study of this configuration is aimed at exploring the aerodynamic interactions that occur during ground proximity of multi-rotors.

7.1 Experimental Setup

The measurements for configuration B3-VTOL have been conducted in the High-Speed Laboratory (HSL) at the TU Delft. Since this configuration deals with the static testing of rotors, no wind tunnel is required. The measurements are therefore conducted in an enclosure of 2x3x2 m^3. In the enclosure, two counter-rotating rotors are installed with their axes perpendicular to a ground plane, see Figure 28. The two-blade twisted rotors comprise a radius of $R = 76.2$ mm, a pitch of 4 inches, and a parabolic tip. The APC-brand rotors are commercially available and their model numbers are APC 6X4E and APC 6X4EP (identical but mirrored, for the counter-rotating configuration).



Figure 28: Side-by-side rotor setup of configuration B3-VTOL.

7.2 Experimental campaigns

Two separate test campaigns have been conducted. First of all, a characterization of the volumetric flow field has taken place. For this, experiments have been performed using three-dimensional large-scale volumetric velocimetry with helium-filled soap bubbles as tracers. In the experiments, both the rotor separation distance and the ground stand-off distance are varied. A second investigation focused on the unsteady flow behaviour around the same setup. Here, 2D time-resolved Particle Image Velocimetry measurements are conducted over a long acquisition time.

7.3 Main results

The back pressure imposed by the ground caused both rotor's wakes to expand radially forming a wall jet. The two wall jets then interact with each other and separate from the ground, generating a fountain-like flow pattern. An illustration of the fountain phenomenon is shown in Figure 29a and b, by the the instantaneous velocity magnitude (blue) and positive axial velocity iso-surfaces (red) for two different ground stand-off distances.

In Figure 29a the fountain remains below the rotor disk and therefore the inflow to the rotors is relatively undisturbed. When the ground stand-off distance is reduced in Figure 29b, the fountain rises over the rotor disk and is re-ingested in the left rotor. Since the rotor wake consists of coherent structures,

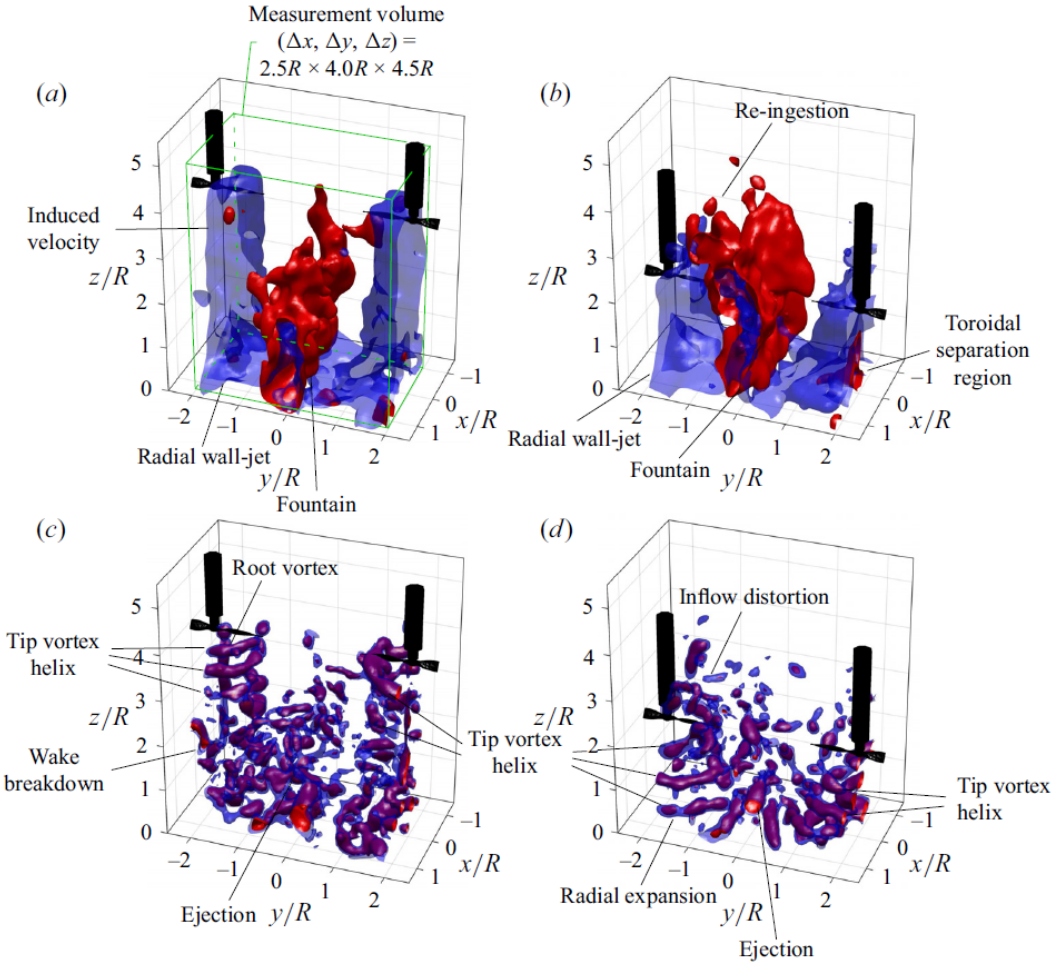

Figure 29: (a) Iso-surfaces of normalized velocity magnitude $V/w_{ind} = 0.5$ (blue) and $w/w_{ind} = 0.25$ (red) for $H/R = 4$ and (b) $H/R = 2$. (c) Iso-surfaces of $\lambda_2 = -60000\,s^2$ (blue) and $\lambda_2 = -90000\,s^2$ (red) for $H/R = 4$ and (d) similar isosurfaces for $H/R = 2$. The measurement volume is illustrated by the green box in (a).

as highlighted by the λ_2-criterion in Figure 29c and d, the inflow is distorted for the lower ground stand-off distance.

Even though the re-ingestion of the fountain is observed to one of the rotors in the time instant presented in Figure 29, the direction of re-ingestion was observed changing back and forth from one rotor to the other. This is illustrated by the two time-series presented in Figure 30.

The top sequence in Figure 30 starting at t_1 captures a relatively stable fountain flow reaching above the rotor disks. Hence, the phenomenon of fountain flow re-ingestion, by one of the two rotors, is minimal. Contradictory to this is the statistically-independent time sequence starting at t_2, shown at the bottom. Here the fountain flow column is shown to drift in lateral direction, resulting in the switching of the re-ingestion from one rotor to the other. An investigation using modal decomposition techniques showed that there dynamic features are observed at an intermittent frequency, which is related to the convective frequency of the re-ingestion loop.

7.4 Main Achievements

The main conclusions for B3-VTOL can briefly be summarized:

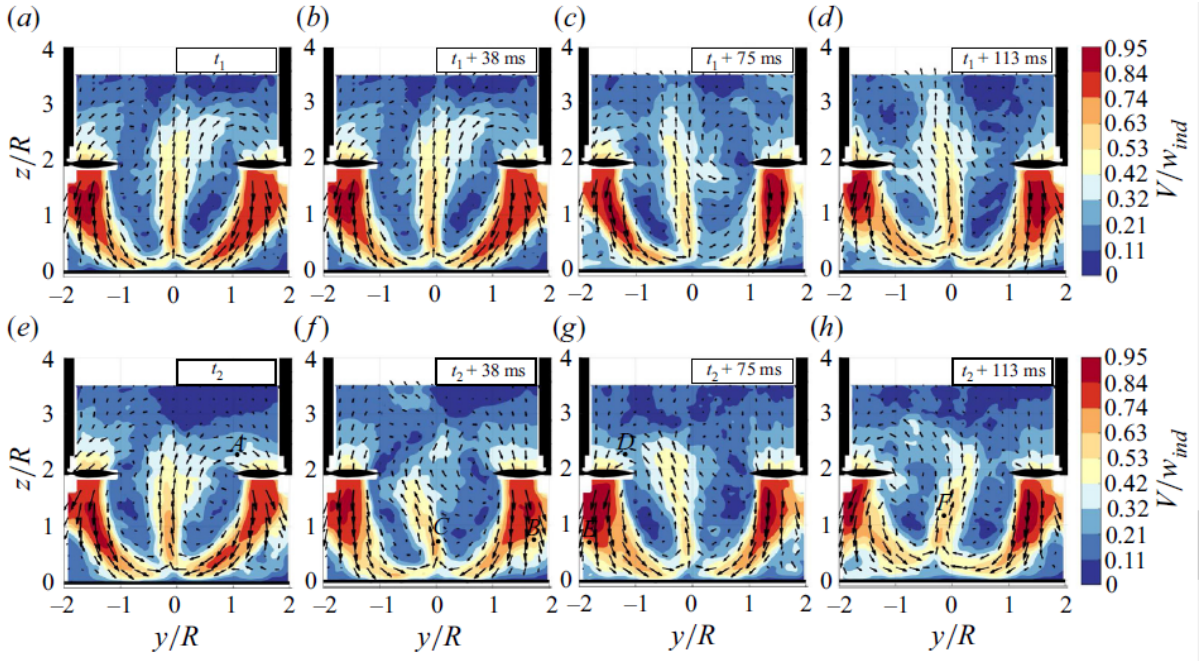

Figure 30: Normalized velocity magnitude contours V/w_{ind} and 2D velocity vectors of two time sequences of sliding averages (ensembles of 100 samples/0.25s), with a temporal increment of $dt = 0.0375$s. The top row series is statistically-independent from the bottom one, with $t_2 = t_1$+1.7 s.

- Experimental studies with volumetric measurements obtained by Lagrangian particle tracking velocimetry and particle image velocimetry, using helium-filled soap bubbles as tracer, has been carried out to investigate the rotor wake characteristics
- Different flow regimes for a side-by-side rotor in ground effect have been identified. These flow regimes depend on a combination of rotor spacing and height over the ground plane.
- In closely spaced rotors, with a tip-to-tip spacing close to zero, the individual rotors wakes form a combined wake before they interact with the ground plane. By increasing the rotor separation to tip-to-tip spacings of at least one rotor radius, an upward flow component known as the fountain flow is created over a line between the two rotors.
- For lower ground stand-off distances, the fountain rises above the rotor disks where it is re-ingested into one of the two rotors. During re-ingestion, velocity fluctuations are increased in the fountain, resulting in more pronounced side-by-side drifting of the column.
- The dynamic features of the fountain flow are observed at an intermittent frequency, which is related to the convective frequency of the re-ingestion loop. Consequently, this intermittent frequency depends on the system parameters (ground stand-off distance and rotor thrust) through the height of the fountain and its characteristic velocity.
- All data has been processed and is available for open access in Zenodo using the following link: `https://doi.org/10.5281/zenodo.7875780`

7.5 Deliverables

The data from the experimental campaigns and the analyses for B3-VTOL have been used in D3.4, D3.6 and D3.7.

7.6 Dissemination

- Dekker, H. N.J. , Ragni, D., Baars, W. J., Scarano, F., & Tuinstra, M. (2021). Three-Dimensional Flow Topology of a Multi-rotor in Ground Effect. *DICUAM* 2021.
- Dekker, H. N., Ragni, D., Baars, W. J., Scarano, F., & Tuinstra, M. (2022). Aerodynamic Interactions of Side-by-Side Rotors in Ground Proximity. *AIAA Journal*, *60*(7), 4267-4277.
- Dekker, H.N.J., Baars, W.J., Scarano, F., Tuinstra, M., & Ragni, D. (2023) Unsteady flow behavior of multi-rotors in ground proximity. *Flow*. In-press

8 Configuration B3-Flap

For B3-FLAP, an over-the-wing propulsion system is experimentally investigated. The investigation focussed on the trade-off between acoustic and aeropropuslive performance that can be achieved by varying the propeller position, and on the aerodynamic and propulsive loading related to the transition from vertical to forward flight conditions.

8.1 Experimental Setup

The experiments for configuration B3-Flap were performed in the Aeroacoustic Wind Tunnel (AWT) facility at the Netherlands Aerospace Centre (NLR) in Marknesse, see Figure 31. A F15 wing model was mounted vertically on a turntable in the closed test section, as shown in the right image of Figure 31. Acoustic transparent walls are used for the acoustic measurements. The wing's chord comprises 240mm and the boundary layer was tripped at 10% chord on both the suction and pressure side. Over the suction side of the wing, a sting was connected to the same turntable as the wing. The sting serves as a support structure for five, span-wise distributed nacelles and aligns each nacelle's axis to the wing's chord direction.

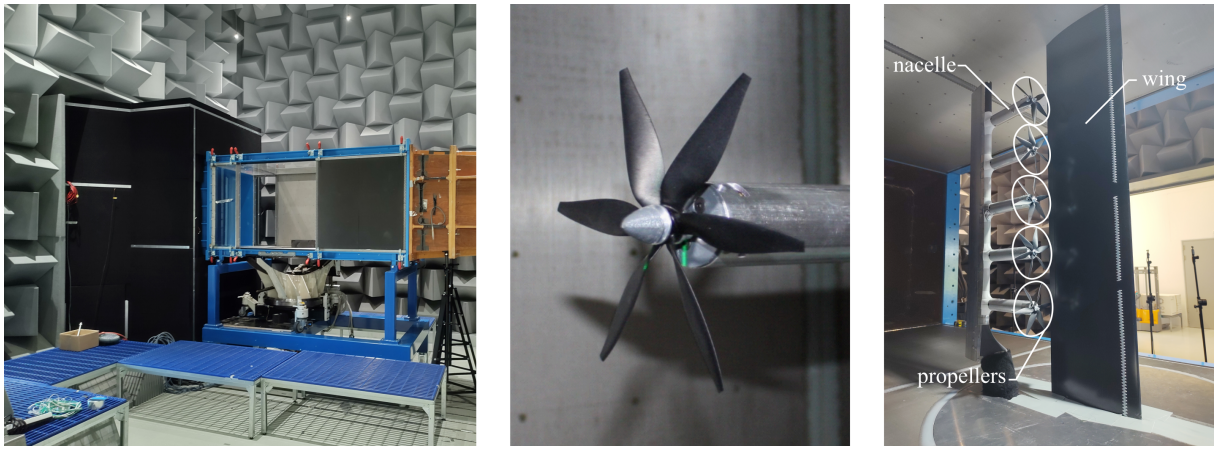

Figure 31: Setup for B3-FLAP in the Aeroacoustic Wind Tunnel (AWT) at NLR-Marknesse

Inside each nacelle, a brushless in-runner motor drives a custom design six-bladed propeller (radius of 63.5 mm) at a shaft frequency of 383 Hz. The blade design of this propeller is based on a benchmarked version for low-Reynolds application derived from a NACA4412 airfoil. The propeller has been manufactured with CNC out of aluminum with 0.02 mm precision, and cured to avoid material relaxation and oxidation.

8.2 Experimental campaigns

The experiments for B3-Flap have been split into three separate test campaigns, with an increasing degree of complexity of the model. First of all, the single isolated propeller is tested, then a single over-the-wing propeller, and finally five distributed propellers over-the-wing. The measurement techniques consisted of integral loads on both the propeller and wing, pressure orifices, microphone measurements, and velocimetry (both planar and stereo).

8.3 Main results

The general flow features of the propeller-wing system are shown in Figure 32 by the velocity magnitude iso-contours and 2D velocity streamlines in a with an offset of 30mm from the propeller axis. Shown is

the data for an advance ratio J of 0.3, corresponding to high thrust conditions, and increasing angle of attack α.

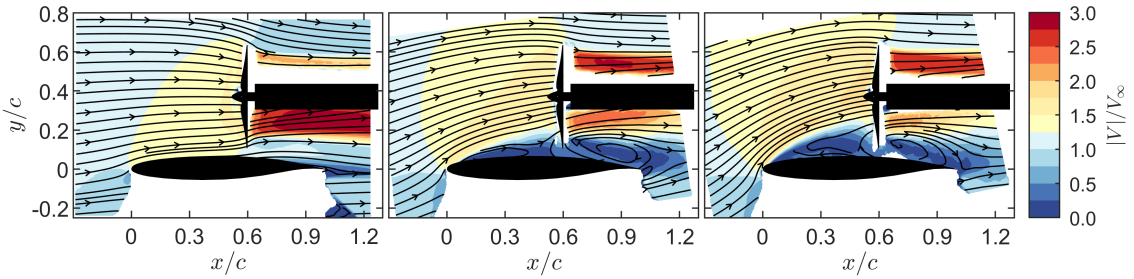

Figure 32: Normalized velocity magnitude contours and 2D streamlines for $\alpha = 0°$, $\alpha = 10°$ and $\alpha = 12°$ for $J = 0.3$ and $x_p/c = 0.6$.

The left image in Figure 32 shows the propeller wing system without any inclination. In this case the propeller accelerates the flow over the wing but the streamtube is separated after the disk. Increasing the angle to $\alpha = 8°$, corresponding to a high lift scenario before the offset of stall for the isolated wing. Here the flow is shown to separate upstream of the propeller, close to the leading edge. Consequently, a flow reversal region between the propeller and wing is occuring. The right image of Figure 32 shows the velocity field for $\alpha = 12°$, the angle at which the isolated wing stalls. Here a similar velocity profile compared to the case of $\alpha = 8°$ is shown, but with more pronounced ingestion of separated flow.

The propeller's induced velocity over the wing increases the wing's lift. This is illustrated by the $c_l - \alpha$ curves for different chordwise propeller positions x_p/c and advance ratios J in Figure 33. The c_l values are computed using loading data from the wing only.

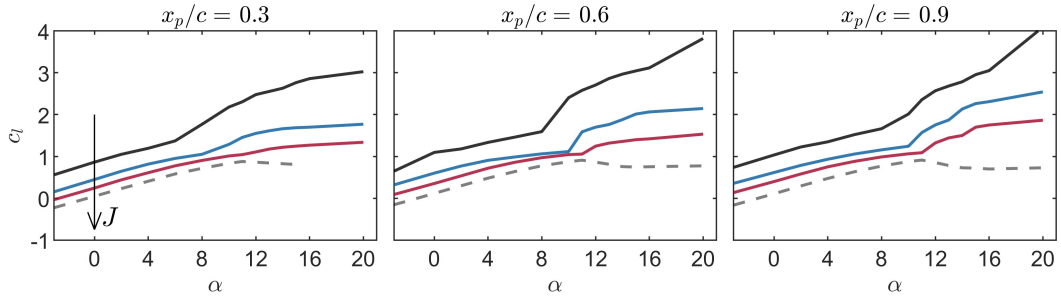

Figure 33: $c_l - \alpha$ curves for $x_p/c = 0.3$ (left),$x_p/c = 0.6$ (middle) ,$x_p/c = 0.9$ (right) for advance ratios of $J = 0.3$ (black), $J = 0.45$ (blue) and $J = 0.6$ (red). The dotted line is the data with the propeller removed.

In Figure 32, a constant lift increase is shown in the isolated wing's pre-stall regime. This lift increases is further enhanced with decreasing advance ratio J and increasing propeller chordwise position x_p/c. At the stall angle for the isolated wing, i.e. $\alpha = 10°$, an additional lift increase is shown for the installed system. Consequently, no abrupt losses of lift are found for this propeller-wing system.

Apart from the increase of the aerodynamic performance, another benefit of over-the-wing propulsion is shielding of propellers noise to reduce the acoustic footprint during flyovers. This is validated using microphone measurements, both at the suction and pressure side of the propeller-wing system, data of which is presented in Figure 34.

In Figure 34a, the noise spectrum of the isolated propeller is compared with the installed configuration. Shown is that the first BPF is increased by 6 dB on the suction side, but decreased by 6 dB on the pressure side compared to the isolated propeller. The sound pressure level of the second and third BPF

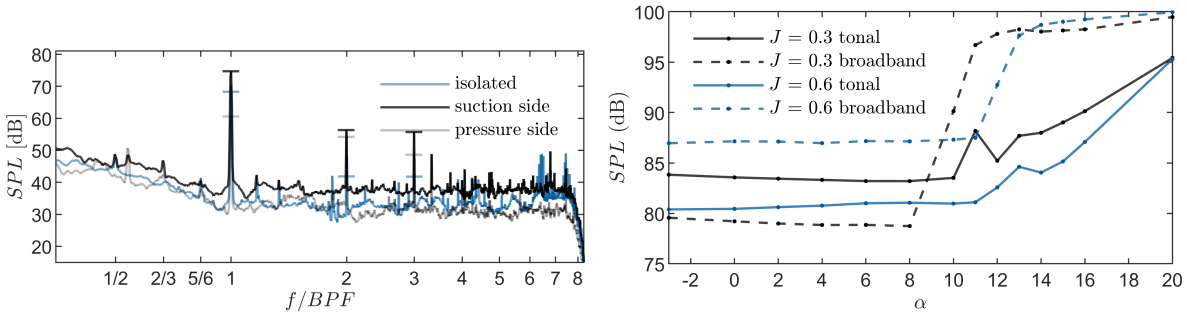

(a) Noise spectrum in the propeller plane for $x_p/c = 0.6$ and $J = 0.3$

(b) Integrated tonal and broadband components in the propeller plane for $x_p/c = 0.6$.

Figure 34: Acoustic data for B3-Flap

are increased on both the suction and pressure side however, which is the result of the flow non-uniformity imposed by the presence of the wing. The integrated broadband and tonal noise levels are presented as a function of the angle of attack in Figure 34b. From this, it becomes apparent that for angles up until $\alpha = 10°$ broadband and tonal contributions to the overall sound pressure level are comparable in magnitude. After further inclination, when the separated flow from the wing is ingested, the noise dramatically increases. The broadband noise increases more suddenly and strongly compared to the tonal noise here. Hence broadband noise becomes dominant at these angles of attack.

8.4 Main Achievements

The main conclusions for B3-FLAP can briefly be summarized:

- The aerodynamic and aeroacoustic installation effect of the over-the-wing propulsion have been investigated in three separate experimental campaigns using integral loading, pressure orifices, microphone, and velocimetry measurements.
- The data shows a decrease in thrust up to 20% compared to the isolated propeller, with a strong dependency on the angle of attack
- The propeller causes flow separation over the wing in high thrust conditions. Furthermore, a flow reversal region between the propeller and the wing's surfaces is formed.
- An increase in lift compared to the isolated wing was found in the pre-stall regime was found which is constant with the angle attack but increases with decreasing advance ratio and increasing propeller chordwise position. An additional lift increase is present in post-stall conditions.
- In cruise, the noise of the 1st BPF is effectively reduced by 6 dB on the pressure side of the wing but increases by 6 dB on the suction side compared to the isolated propeller
- A large increase in noise (18 dB) is present for angles of attack over the isolated wing's stall angle, caused by ingestion of the separated boundary layer.
- All data has been processed and is available for open access in Zenodo using the following link: `https://doi.org/10.5281/zenodo.7875780`

8.5 Deliverables

The data from the experimental campaigns and the analyses for B3-FLAP have been used in D3.2, D3.4, D3.6 and D3.7.

8.6 Dissemination

- Dekker, H., Tuinstra, M., Baars, W. J., Scarano, F., & Ragni, D. (2023). Aeropropulsive Performance Modelling of Over-The-Wing Propulsion at Incidence. In *AIAA AVIATION 2023 Forum* (p. 3355).
- Dekker, H., Brouwer, H., Kok, J., Laban, M., & Tuinstra, M. (2023). Tonal noise measurements and simulations of an Over-The-Wing propeller. In *AIAA AVIATION 2023 Forum* (p. 3358).

9 Configuration C

The experimental aerodynamic and acoustic data for configuration C, comprising both single and contra-rotating propeller loads and emitted noise, were measured within the ALCOVES anechoic facility at the von Karman Institute for Fluid Dynamics in Belgium.

9.1 Experimental Setup

The sketch of the setup and some dimensions are illustrated in Figure 36. The mockup is composed of two independent propeller systems: *Propeller 1* indicates the front propeller and *Propeller 2* the rear one. The two test stands are placed behind each other and aligned on the same axis to minimize aerodynamic interactions and reduce acoustic scattering. The stand placed at the rear is designed with a long shaft supported with several bearings and passes through the first stand. The axial spacing between the front and rear propellers d varies in a range of 2 cm to 4 cm by moving the front propeller on the long shaft.

The front stand is composed of the same elements, with a hollow shaft through which the rear motor shaft passes. Furthermore, the long shaft aligns and holds together the rotor and the stator of the front motor. The hollow shaft is also aligned with means of bearings placed between it and the long shaft. Moreover, the presence of the two test stands allows independent change of the RPM and sense of rotation of the two propellers. Hence, both co- and contra-rotating configurations can be analyzed.

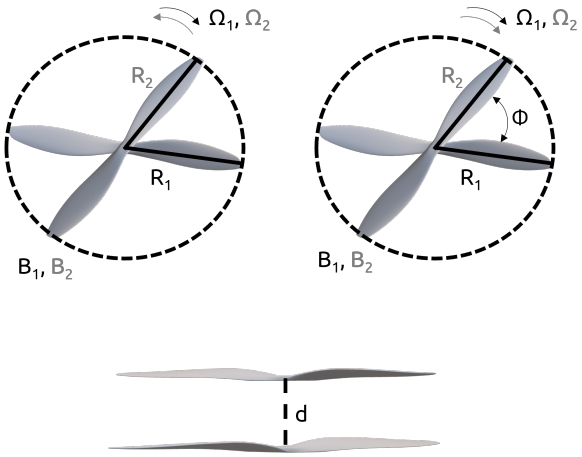

Figure 35: Exploitable configurations: Ω indicates the rotational speed, R is the blade radius, B is the blade numbers and d is the spacing between front and rear propeller.

Acoustic measurements were conducted using three G.R.A.S. 40PL microphones, as illustrated in Figure 37. The microphone positions were defined with reference to a Cartesian coordinate system centered at the midpoint of the rear propeller, specifically the disk of *Propeller* 2. In this coordinate system, the z-axis was oriented positively along the rotor axis in the upstream direction, the y-axis represented the downstream direction along the middle of the disk, and the x-axis completed the right-hand rule system.

Mic 0 was positioned within the $x - z$ plane, aligned along the negative x-axis, and situated at a distance of 65 cm from the origin. Mic 1 was located upstream of the rotor at an inclination of 10.6° and a distance of 56 cm from the rotor axis. Additionally, Mic 2 was placed along the negative y-axis, with a separation of 83 cm from the origin. The microphone arrangement described above is visualized in Figure 38 for reference.

9.2 Experimental campaigns

The experiments were systematically planned according to the commissioning procedure. Initially, background noise measurements of Motor 1 and Motor 2 across a range of 4000 to 7000 RPM, cooling line, and

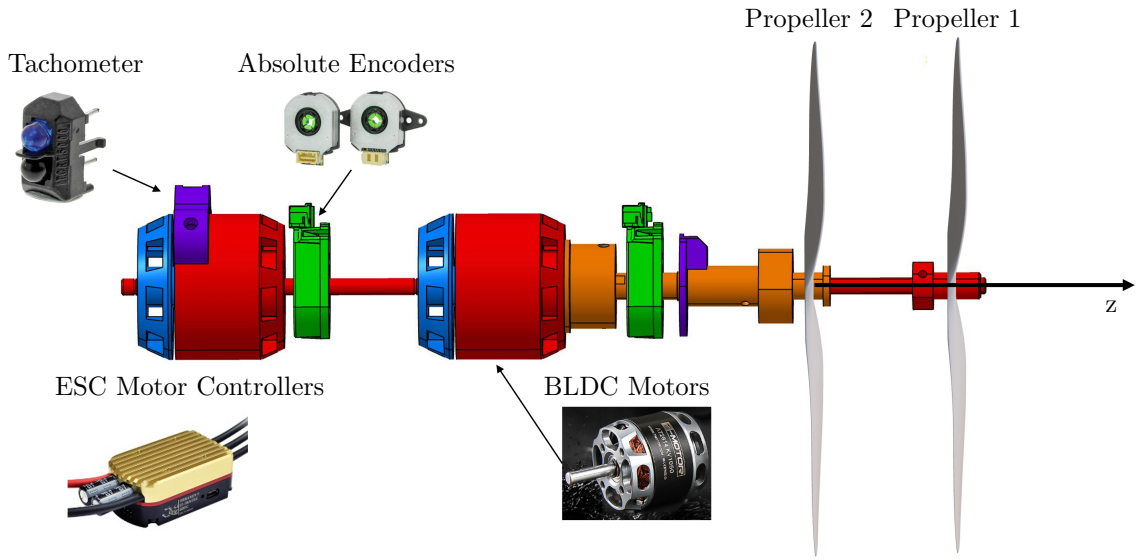

Figure 36: CAD scheme of the coaxial rotor mock-up.

anechoic room were acquired. Subsequently, the analysis of wake re-circulation noise levels was performed with Mejzlik 2-blade and 3-blade propellers, as well as the DJI 9450 propeller across a range of 4000 to 7000 RPM. Finally, an experimental dataset for the aerodynamic and acoustics characterization of single and coaxial Mejzlik 2-blades propellers has been recorded and published on the open-source ZENODO platform [6]. The configurations are shown in Tables 11 and 12.

Table 11: Motor and single propellers test configurations

Configurations	RPM
Motor 1	4000, 5000, 5250, 6000, 7000
Motor 2	4000, 5000, 6000, 7000
DJI 9450	4000, 5000, 5250, 6000, 7000
Mejzlik 2-blades	4000, 4100, ..., 7000

Table 12: Coaxial contra-rotating propellers test configurations

d [cm]	RPM
2	4000, 4100, ..., 7000
2.5	4000, 4100, ..., 7000
3	4000, 4100, ..., 7000
3.5	4000, 4100, ..., 7000
4	4000, 4100, ..., 7000

9.3 Main results

Figure 39 shows the SPL measured at Mic 0, indicated in Figure 38, of anechoic room background, cooling system, motors alone, and isolated Mejzlik 2-blades propellers operating at 6000 RPM. In the legend, *Motor 1* and *Motor 2* refer to the motors driving the front and rear propellers, respectively. The background noise, represented by the gray line, exhibits an average value of 4.5 dB. Hence, it is considered negligible and does not significantly disturb the measurements. Conversely, the cooling system generates a broadband noise spectrum with an average value of 33 dB. Although this noise contributes to the overall

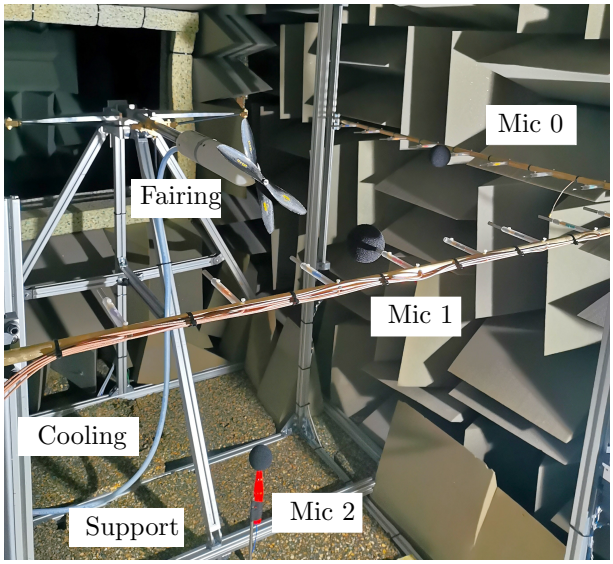

Figure 37: Fairing, cooling hose, supporting stand and microphones setup in the anechoic room ALCOVES.

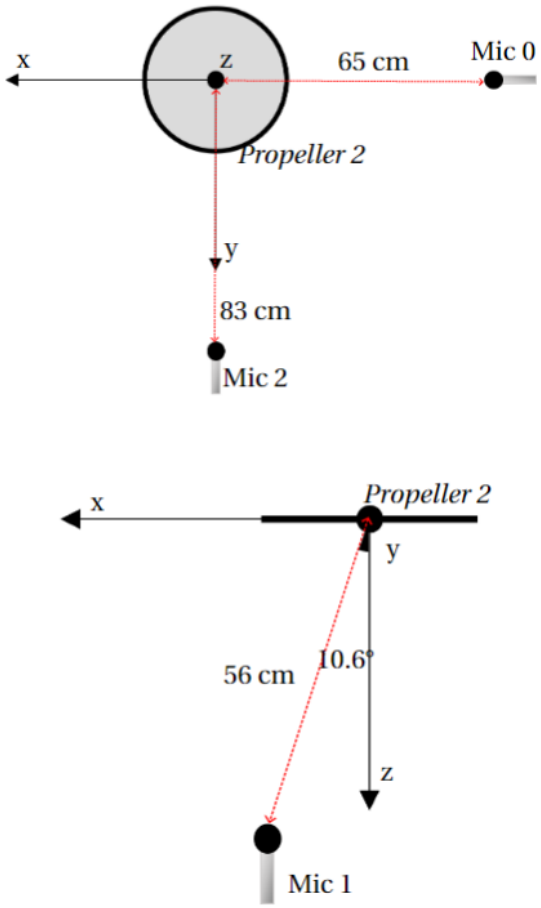

Figure 38: Configuration of microphones in ALCOVES.

acoustic emissions, the examination of individual components reveals that it remains lower in intensity compared to other sources. Above all, it affects the broadband portion of the spectrum. To ensure consistency throughout the measurements, tests were conducted under a fixed input pressure imposed at the pressure line. Regarding the tonal peaks, *Motor 2* exhibits a noise level that is 22 dB higher than *Motor 1* at the first Blade Passage Frequency (BPF). However, the motor noise does not significantly influence the noise generated by the propellers alone. Specifically, at the first BPF, the SPL of the front and rear propellers shows 1 dB of difference. The noise generated by the propellers at the BPF harmonics is shown to be 62 dB at the 2nd Blade Passage Frequency (BPF), decreasing to 55 dB at the 3rd BPF, and further to 51 dB at the 4th and 5th BPFs. Eventually,the background noise analysis suggests that the propeller noise is dominant.

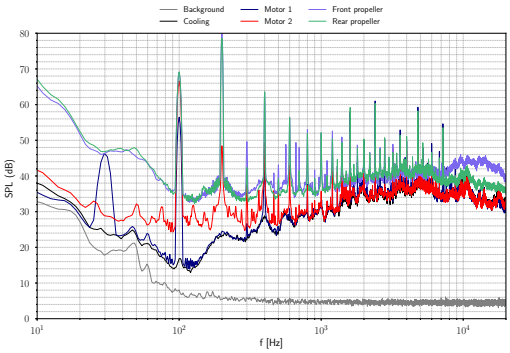

Figure 39: SPL of anechoic room, cooling system, motors alone and isolated Mejzlik 2-blades propellers at 6000 RPM measured at Mic 0.

A critical aspect of the analysis involves investigating the possible presence of wake re-circulation. Hence, a set of experiments was performed under different configurations for isolated propellers (Table 11). Figure 40 illustrates a spectrogram that effectively demonstrates this phenomenon. The specific case features the Mejzlik 2-blade propellers operating at 6000 RPM. The measurements were taken at Mic 0 over a 30 second interval. The initial 10 second of the spectrogram captures the ramp-up phase of the setup, during which the propeller speed increases from an initial RPM to a peak value before the controller stabilizes it at the desired RPM. Over the course of the 30 second interval, the tonal peaks corresponding to the Blade Passage Frequencies (BPFs) are clearly evident. The spectrum does not reveal any rise in either tonal or broadband noise levels over time. A possible explanation may be attributed to the design of the anechoic room itself. It is possible that the wake generated by the propellers is effectively evacuated and perhaps confined to the rear of the test room. This finding suggests that the presence of wake re-circulation may not be significant under these experimental conditions.

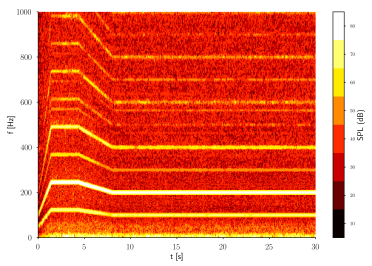

Figure 40: SPL spectrogram of isolated Mejzlik 2-blades propellers at 6000 RPM measured at Mic 0.

In Figure 41, thrust measurements obtained using the loadcell are presented for the Mejzlik 2-blade propeller in two hover configurations: isolated and contra-rotating, with varying distances between 2 and 4 cm. The experiments involved incrementally increasing the RPM from 4000 to 7000. The results

clearly demonstrate a substantial increase in thrust for the isolated rotor configuration, ranging from 5 N to 15 N as the RPM is elevated, according to the propeller's capacity to generate higher thrust levels as the rotational speed increases. Finally, Figure 42 shows SPL comparison measured for isolated and contra-rotating Mejzlik 2-blades propeller at a distance of 3 cm (baseline configuration).

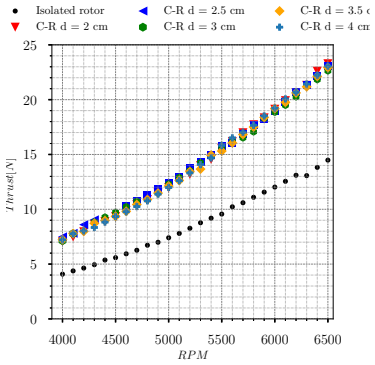

Figure 41: Thrust vs RPM for isolated and contra-rotating Mejzlik 2-blades propeller.

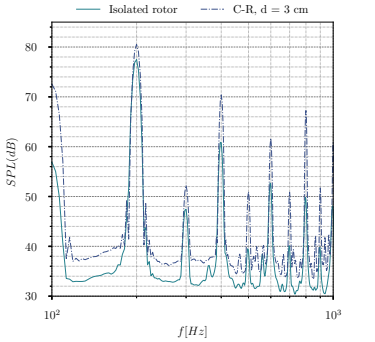

Figure 42: SPL measured at $Mic1$ for isolated and contra-rotating Mejzlik 2-blades

9.4 Main Achievements

A summary of the experimental findings is briefly reported here:

1. The background noise levels of external components were observed to be lower than the noise emitted by the propeller, highlighting the propeller as the primary noise source.
2. Wake re-circulation noise levels were found to be non-significant, indicating that they do not contribute significantly to the overall acoustic noise.
3. Analysis of thrust curves for both isolated and contra-rotating propellers as a function of RPM demonstrated a consistent increase in thrust with higher rotational velocity.
4. The Sound Pressure Level (SPL) for the contra-rotating propeller exhibited higher-frequency tones compared to the isolated propeller configuration, aligning with expected acoustic differences.

9.5 Deliverables

The data from the experimental campaigns and the analyses for Configuration C have been used in D3.6 and D3.7.

9.6 Dissemination

All data have been processed and are available for open access in Zenodo using the following link: `https://doi.org/10.5281/zenodo.8334930`

10 Conclusion

In conclusion, the extensive experimental campaigns realized on Tasks 3.1, 3.2, and 3.3 have achieved valuable insights into boundary layer ingestion, propeller-wing interactions, and aeroacoustic characteristics of propulsive systems. With data gathered from multiple configurations and experimental setups, the Work Package has successfully generated comprehensive datasets that are essential in the numerical simulations in WP4 and also guide the optimization efforts in WP5. These experiments, conducted by a collaborative effort of multiple partners, have paved the way for a deeper understanding of flow and noise mechanisms, providing crucial validation for both low- and high-fidelity numerical methods. The conclusion of these efforts represents a significant step forward in advancing our knowledge of aeroacoustics and propulsive systems, setting the stage for further advancements in the field.

References

[1] Leandro D. de Santana, Martinus P. Sanders, Cornelis H. Venner, and Harry W. Hoeijmakers. The utwente aeroacoustic wind tunnel upgrade. pages 1–12, 2018. Description of the upgraded acoustic wind tunnel in the University of twente (currently the open flow is working).

[2] Jochen Wild. Mach and reynolds number dependencies of the stall behavior of high-lift wing-sections. *Journal of Aircraft*, 50(4):1202–1216, 2013.

[3] Nando van Arnhem, Reynard de Vries, Tomas Sinnige, Roelof Vos, Georg Eitelberg, and Leo LM Veldhuis. Engineering method to estimate the blade loading of propellers in nonuniform flow. *AIAA Journal*, 58(12):5332–5346, 2020.

[4] Reynard de Vries, Nando van Arnhem, Tomas Sinnige, Roelof Vos, and Leo L.M. Veldhuis. Aerodynamic interaction between propellers of a distributed-propulsion system in forward flight. *Aerospace Science and Technology*, 118:107009, 11 2021.

[5] M. Sunyach, B. Bruiel, and G. Comte-Bellot. Performance of the high speed anechoic wind tunnel at lyon university. *NASA Technical Report*, 1986.

[6] Erica Gallo, Julien de Decker, Pauline Haezebrouck, Alessandro Zarri, and Christophe Schram. H2020 enodise: Experimental dataset of configuration c vki, doi:10.5281/zenodo.8334930, May 2023.